Criteria for extensional necking instability in complex fluids and soft solids. Part I: imposed Hencky strain rate protocol.

D. M. Hoyle* and S. M. Fielding†
Department of Physics, University of Durham, Science Laboratories, South Road, Durham, DH1 3LE, United Kingdom
(Dated: November 22, 2016)

We study theoretically the necking dynamics of a filament of complex fluid or soft solid in uniaxial tensile stretching at constant imposed Hencky strain rate $\dot{\epsilon}$, by means of linear stability analysis and nonlinear (slender filament) simulations. We demonstrate necking to be an intrinsic flow instability that arises as an inevitable consequence of the constitutive behaviour of essentially any material (with a possible rare exception, which we outline), however carefully controlled the experimental conditions. We derive criteria for the onset of necking that are reportable simply in terms of characteristic signatures in the shapes of the experimentally measured rheological response functions, and should therefore apply universally to all materials. As evidence of their generality, we show them to hold numerically in six popular constitutive models: the Oldroyd B, Giesekus, FENE-CR, Rolie-Poly and Pom-pom models of polymeric fluids, and a fluidity model of soft glassy materials. Two distinct modes of necking instability are predicted. The first is relatively gentle, and sets in when the tensile stress signal first curves downward as a function of the time t (or accumulated strain $\epsilon = \dot{\epsilon}t$) since the inception of the flow. The second is more violent, and sets in when a carefully defined 'elastic derivative' of the tensile force first slopes down as a function of t (or $\dot{\epsilon}$). In the limit of fast flow $\dot{\epsilon}\tau \to \infty$, where τ is the material's characteristic stress relaxation time, this second mode reduces to the Considère criterion for necking in solids. However we show that the Considère criterion fails to correctly predict the onset of necking in any viscoelastic regime of finite imposed $\dot{\epsilon}\tau$, despite being widely discussed in the complex fluids literature. Finally, we elucidate in detail the way in which these modes of instability manifest themselves in entangled polymeric fluids (linear polymers, wormlike micelles and branched polymers). In particular we demonstrate four distinct regimes of necking behaviour as a function of imposed strain rate, consistent with master curves in the experimental literature.

I. INTRODUCTION

Extensional flows provide a crucial benchmark for constitutive theories of the rheology of complex fluids. Under conditions of constant imposed Hencky strain rate, material elements separate exponentially quickly and so subject the fluid's underlying microstructure (polymer chains, wormlike micelles, *etc.*) to much more severe reorganisation than is typically experienced in shear. In consequence, many nonlinear flow features manifest themselves only in extension: *e.g.*, the extensional strain hardening exhibited by many polymeric fluids. Extensional flows are therefore highly sensitive to the underlying fluid microstructure, and prove important in discriminating between competing constitutive theories.

Key aims of any constitutive model are to predict a fluid's stress response as a function of applied strain history (or vice versa), in both shear and extension. In the literature, many theoretical calculations make the simplifying assumption that the flow field remains spatially uniform in any given flow protocol. In practice this assumption may prove valid, to good approximation, in some region of a carefully designed flow cell. Near uniform simple shear may obtain in a narrow gap Couette device, for example. Likewise a region of near uniform extension may obtain in the vicinity of the central stagnation point of a cross slot device [1, 2], or in the central part of a hyperbolic contraction flow cell [3].

However for many complex fluids, in many flow situations, conditions of uniform rheometric flow prove unattainable – or at least unsustainable – as a matter of fundamental principle, even in the most carefully designed flow devices, as an unavoidable consequence of a flow instability inherent to the fluid's constitutive response. Under an imposed shear, for example, the phenomenon of shear banding arises widely as a consequence of a flow instability associated with a regime of negative slope in the underlying constitutive curve of shear stress as a function of shear rate. When performing calculations to compare with bulk measurements, it is then crucial to take this heterogeneity into account by removing any assumption of uniform flow in the calculations. Experimentally, spatially resolved velocimetry becomes necessary to ascertain the local constitutive response in each band separately.

To characterise a fluid's extensional rheology, a common experiment consists of stretching out in length an initially undeformed cylindrical filament (or rectangular sheet) of the material. For a review of filament stretching techniques, see [4] and references therein. In stretching at constant imposed Hencky strain rate $\dot{\epsilon}$, the extensional stress growth coefficient $\eta_{\rm E}^{+}(t,\dot{\epsilon})$ records the extensional (tensile) stress $\sigma_{\rm E}^{+}(t,\dot{\epsilon})$, normalised by $\dot{\epsilon}$, as a function of the time t (or accumulated strain $\epsilon = \dot{\epsilon}t$) since the inception of the flow. If this quantity can be measured to steady state, in some part of the sample at least, the steady tensile stress plotted as a function of applied strain rate, obtained in a series of stretching experiments per-

formed at different strain rates, then gives the extensional constitutive curve, or flow curve, $\sigma_E(\dot{\epsilon})$.

Another common protocol comprises stretching a filament at constant tensile stress σ_E [5–7]. This typically allows a fluid to attain a steady flow more quickly than under conditions of constant strain rate, giving readier access to the constitutive curve [8]. Stretching at constant tensile force F provides a more natural mimic of some industrial processes, such as fibre spinning [9, 10].

Even in the most carefully performed filament stretching experiments, however, almost ubiquitously observed is the onset of heterogeneous deformation. Typically (in a filament stretching rheometer at least) the central region of the filament, furthest from the sample ends, develops a higher strain rate than the globally applied one and thins more quickly than the sample as a whole. This eventually causes the filament to fail altogether, aborting the experimental run. It has been seen in linear polymers [11], branched polymers [12, 13], associative polymers [14], wormlike micelles [15], bubble rafts [16], and dense colloidal suspensions [17]. It arises in all common stretching protocols, including at constant tensile stress [18], constant applied Hencky strain rate [13, 19], and following a finite Hencky strain ramp [20]).

Two qualitatively different modes of failure are widely reported [21–26]. In slow stretching, failure typically occurs via a process of ductile necking in which the variations in cross sectional area that develop along the filament's length are relatively gradual. Faster stretching experiments typically cause more dramatic failure in which the sample sharply rips across its cross section in a 'rupture' or 'fracture' event. (Indeed, it is unclear whether there exists a distinction between the 'rupture' that is often refered to experimentally, and 'fracture'. We prefer the term 'fracture' in refering to these more dramatic events in fast stretching.)

Experimentally, the occurrence of necking (or fracture) presents a significant technical challenge to characterising a material's extensional rheology. This is true even before the filament finally fails, because the flow field becomes heterogeneous and therefore renders the measurement of a material's local, homogeneous material response functions more challenging. In particular, the extensional strain rate in the necking part of the sample increases above the globally applied one in a manner that is a priori unpredictable. A comparison of experimental data with the results of calculations that assume a homogeneous flow therefore becomes much more difficult.

To overcome this difficulty, feedback strategies have been developed that monitor the strain rate in the necking region and responsively reduce the globally applied strain accordingly, to keep the strain rate in the neck temporally constant. Knowledge of the tensile force divided by the local area in the neck then gives the time-dependent local tensile stress at the given, feedback-controlled constant local strain rate [8, 27, 28]. Such techniques can be thought of as the counterpart in extensional rheometry of performing spatially resolved velocimetry in shear banded flows, with the additional feature of actively controlling the flow by feedback. However successful such strategies in temporarily stabilising a constant strain rate in the neck, though, it seems highly unlikely that necking could be avoided altogether by any feedback algorithm, being (as we shall show in what follows) a flow instability intrinsic to the material's constitutive behaviour.

With this experimental backdrop in mind, the aim of this work is to study theoretically the onset of necking in filament stretching of complex fluids and soft solids under conditions of constant imposed Hencky strain rate. (In a separate manuscript[29], we consider necking at constant imposed tensile stress or tensile force.) Starting with a time-dependent "base state" corresponding to a uniform cylinder being stretched, we perform a linear stability analysis for the dynamics of (initially) small perturbations in the cylinder's cross sectional area, to determine the onset of necking. We then perform nonlinear simulations to elucidate the dynamics once the necking heterogeneity has attained a finite amplitude, beyond the linear regime. For definiteness we consider a cylindrical filament in uniaxial stretching, though the criteria that we shall derive also apply to planar extension.

Our objectives are threefold. First, we seek to demonstrate the phenomenon of necking to be a flow instability that arises as an inevitable consequence of the constitutive behaviour of essentially any complex fluid or soft solid, however carefully the experiment is performed, unavoidably leading to a heterogeneous extensional flow field along the filament. (In this sense, necking can be viewed as an extensional counterpart of the banding instability that is widely seen in shear.)

Second, we derive criteria for the onset of necking that are universal to all complex fluids and soft solids, and are reportable simply in terms of characteristic signatures in the shapes of the experimentally measured material response functions of tensile stress σ_E^+ and/or tensile force F as a function of the time (or accumulated strain) since the inception of the flow. We shall first derive these by means of analytical linear stability calculations performed within a constitutive model of a highly generalised form. We then confirm their generality by numerical simulations in six concrete choices of constitutive model: the phenomenological Oldroyd B, Giesekus and FENE-CR models; the microscopically motivated Rolie-Poly model of entangled linear polymers and wormlike micelles; the Pom-pom model of entangled branched polymers; and a simplified fluidity model of soft glassy materials (foams, emulsions, dense colloids, microgels, *etc.*), which display a yield stress and rheological ageing [30–32].

Third, we seek to elucidate the way in which our universal criteria manifest themselves in those three major classes of complex fluids: in entangled linear polymers and wormlike micelles; in entangled branched polymers; and in soft glassy materials. In the context of entangled polymers, a particular objective is to demonstrate the tube theory of polymer rheology, with chain stretch

and convective constraint release, to be capable of capturing all the features of a widely discussed experimental master-curve of the strain at which a sample fails as a function of imposed strain rate. In ageing soft glassy materials, we demonstrate that the sample fails by one of two qualitatively different modes of necking, according to the sample age at the time stretching commences.

Commonly discussed in the literature as a predictor for the onset of necking is the Considère criterion [33, 34]. This predicts necking to set in when the tensile force attains a maximum as a function of the accumulated strain, then subsequently declines. It was originally put forward in the context of solid mechanics, for which it is indeed appropriate to take the accumulated strain ϵ as the only relevant deformation variable. For a complex fluid, however, also crucial is the strain *rate* $\dot{\epsilon}$ at which stretching is performed, relative to the inverse characteristic relaxation time $1/\tau$ of the fluid in question. In view of this there is no reason, a priori, for the Considère criterion to apply to complex fluids. Indeed, our calculations will demonstrate that it performs poorly in predicting the onset of necking at low to moderate imposed strain rates (compared to $1/\tau$). It does, however, compare quite well with experiments [11, 21] and simulations [35, 36] at high strain rates $\dot{\epsilon}$. Indeed this is to be expected, because viscoelastic fluids tend towards a solid-like response in the regime $\dot{\epsilon}\tau \gg 1$. In important contrast, the criteria for the onset of necking offered in this work are valid not only in this fast flow regime, but apply across the full range of flow rates from slow to fast. We shall also demonstrate the way in which one of our criteria reduces to the Considère criterion in the limit of fast flow $\dot{\epsilon}\tau \to \infty$.

An early insightful attempt to consider the importance of both strain and strain rate in the onset of necking can be found in [37]. Stability analyses were later performed for Newtonian and Maxwell fluids in[38], and in the Oldroyd B and FENE-CR models in [39, 40]. A scaling theory based on a critical recoverable strain was put forward in [41, 42]. An empirical criterion for rupture was offered in [43]. Direct numerical simulations of necking have been performed within constitutive models of polymers [4, 44, 45], wormlike micelles [46], and amorphous elastoplastic solids [47].

The criteria that we discuss in what follows were first outlined in [48] in the context of polymeric fluids and in [49] in the context of soft glassy materials respectively. The purpose of the present manuscript is to give a much more detailed explanation of the criteria announced in those earlier Letters, and comprehensive numerical evidence supporting them.

Our focus will be on the onset of necking in a highly viscoelastic filament of sufficiently large radius that bulk viscoelastic stresses dominate surface effects. Accordingly, we set the surface tension to zero in most of our calculations. We therefore do not address capillary breakup as studied in CaBeR rheometers [10, 50–55]. However, towards the end of the paper we shall return to incorporate surface tension and show that it affects our results only in the regime of very slow strain rates.

All our calculations are performed within a slender filament approximation in which the wavelengths of any variations along the filament's length are taken as long compared to the filament radius. Our approach therefore cannot capture the details of the final pinchoff of any neck [56, 57], nor can it capture a fracture mode in which the filament sharply rips across its cross section [47, 58, 59]. Such phenomena are deferred to future study. It is worth noting, however, that we might expect the violent necking predicted below in fast flows to be replaced by a sharp fracture event in any fully 3D simulation capable of capturing this.

So far, we have discussed the onset of a heterogeneous profile along the filament in terms of a true material instability (necking). It is important to note, however, that even before a true necking instability arises, some narrowing of the central region of the filament relative to that near each endplate is to be expected because of the boundary condition that prevents the fluid from slipping at the plates, and therefore prevents those parts of the sample nearest the plates from being properly stretched. Indeed, below we shall discuss the way in which this initial heterogeneity induced by the flow geometry acts as a seed that is then picked up and hugely amplitude by the true material necking instability. However we also note that, even in a thought experiment in which the effect of the boundary conditions could be removed altogether (for example by perfectly cothinning the endplates concurrently to match the changing diameter of the filament), the necking instability would be seeded by other sources of heteroeneity (such as initial sample imperfection) and could not be avoided. Our calculations with periodic boundary conditions below will confirm this.

The paper is structured as follows. We start in Sec. II with a preamble concerning measures of extensional force and stress that are commonly reported in the experimental literature. In Sec. III we discuss the constitutive models and flow protocol to be studied throughout the paper. In Sec. IV we outline in general terms the procedure of our linear stability analysis for the onset of necking. In Sec. V we use this analysis, within a constitutive model of highly general form, to derive fluid-universal criteria for the onset of two qualitatively different modes of necking instability. We discuss the rheological signature of these modes in the form of characteristic features in the shapes of the material response functions plotted versus the time (or accumulated strain) since the inception of the flow. To confirm the validity of these general criteria, we then perform in Sec. VI numerical calculations of the linearised necking dynamics within six widely used constitutive models and show the criteria to indeed hold within them. We further discuss in more detail the way the criteria manifest themselves in three important classes of complex fluid: entangled linear polymers and wormlike micelles, entangled branched polymers, and soft glasses. In Sec. VII we perform nonlinear simulations to study the dynamics once the neck has developed to attain

a finite amplitude. Sec. VIII contains our conclusions.

II. MEASURES OF FORCE, STRESS AND STRAIN

Key variables measured as a function of the time t (or accumulated strain $\epsilon = \dot{\epsilon}t$) during filament stretching at constant imposed Hencky strain rate $\dot{\epsilon}$ are the tensile force $F(t)$, and the tensile stress, *i.e.*, the tensile force per unit cross sectional area. In fact three different tensile stress measures are commonly reported experimentally, according to which area variable is used in the denominator:

(a) The engineering stress is defined at any time t as the force $F(t)$ normalised by the cross sectional area, A, of the filament at the *start* of the run, $\sigma^+_{E,\mathrm{eng}}(t) = F(t)/A(0)$. Further dividing this by the constant value of the imposed Hencky strain rate gives the engineering stress growth coefficient $\eta^+_{E,\mathrm{eng}}(t) = F(t)/A(0)\dot{\epsilon}$. It is important to note, however, that this quantity does not properly characterise the tensile stress, because it does not allow for the filament's (on average) exponentially decreasing cross sectional area $A(t) = A(0)\exp(-\epsilon)$ as a function of the accumulating strain ϵ. In fact, the engineering stress should properly be recognised as a measure of the time-dependence of the tensile force, normalised by the initial area $A(0)$.

(b) The apparent tensile stress is defined at any time t as the force $F(t)$ normalised by the cross sectional area $A_{\mathrm{hom}}(t) = A(0)L(0)/L(t) = A(0)\exp(-\epsilon)$, as calculated by supposing that the filament has remained perfectly uniform up to that time, without any necking yet having occurred. This gives an apparent stress $\sigma^+_{\mathrm{E,app}}(t) = F(t)/A_{\mathrm{hom}}(t)$ and a corresponding apparent stress growth coefficient $\eta^+_{\mathrm{E,app}}(t) = F(t)/\dot{\epsilon}A_{\mathrm{hom}}(t)$. As a measure of the tensile stress this is a significant improvement on the engineering stress, in accounting for the overall exponential decrease in the filament's cross sectional area. However it still does not properly report the tensile stress once necking occurs, because the cross sectional area then varies along the filament's length.

(c) The true tensile stress at any time t and location z along the filament's length is defined as the force $F(t)$ divided by the actual cross sectional area of the filament at that point, $A(z,t)$, giving $\sigma^+_{\mathrm{E}}(z,t) = F(t)/A(z,t)$. (Note that although the *stress* may vary as a function of position along the filament's length, the *force* must remain uniform by force balance at the low Reynolds number flows of interest here.) The corresponding true stress growth coefficient $\eta^+_{\mathrm{E}}(z,t) = F(t)/\dot{\epsilon}A(z,t)$. To track the evolution of this quantity at some location z requires not only a measurement of the tensile force, but also of the evolving cross sectional area at that location [8, 27, 60].

In seeking to compare our numerical results with experimental data, we shall sometimes show data for the apparent stress growth coefficient $\eta^+_{\mathrm{E,app}}(t)$, to make contact with experiments that do not explicitly track the effect of necking on the cross sectional area; and sometimes for the true stress growth coefficient $\eta^+_{\mathrm{E}}(z_{\mathrm{mid}},t)$, to make contact with experiments that do track the time-evolution of the cross sectional area in the developing neck. We use the value $z_{\mathrm{mid}} = L(t)/2$ because in all our simulations the neck develops at the filament's midpoint.

Finally, in any experiment where necking occurs the strain and strain rate will vary along the filament: $\epsilon = \epsilon(z,t)$ and $\dot{\epsilon} = \dot{\epsilon}(z,t)$. The averages of these along the filament correspond to the globally imposed strain and strain rate, $\bar{\epsilon}$ and $\dot{\bar{\epsilon}}$ respectively, and are often called the nominal Hencky strain and nominal Hencky strain rate.

III. MODELS AND FLOW GEOMETRY

A. Mass balance and force balance

We write the total stress $\boldsymbol{T}(\boldsymbol{r},t)$ at time t in a fluid element at position $\boldsymbol{r}$ as the sum of a viscoelastic contribution $\boldsymbol{\Sigma}(\boldsymbol{r},t)$ from the internal fluid microstructure (polymer chains, wormlike micelles, emulsion droplets, *etc.*), a Newtonian contribution of viscosity η, and an isotropic contribution with a pressure $p(\boldsymbol{r},t)$:

$$\boldsymbol{T} = \boldsymbol{\Sigma} + 2\eta\boldsymbol{D} - p\boldsymbol{I}. \tag{III.1}$$

The Newtonian contribution may arise from the presence of a solvent, and/or from any polymeric (or other viscoelastic) degrees of freedom considered fast enough not to be ascribed their own dynamics. The symmetric strain rate tensor $\boldsymbol{D} = \frac{1}{2}(\boldsymbol{K} + \boldsymbol{K}^T)$ where $K_{\alpha\beta} = \partial_\beta v_\alpha$ and $\boldsymbol{v}(\boldsymbol{r},t)$ is the fluid velocity field.

We consider the creeping flow limit of zero Reynolds number, in which the condition of force balance requires the stress field $\boldsymbol{T}(\boldsymbol{r},t)$ to be divergence free:

$$\boldsymbol{\nabla}\cdot\boldsymbol{T} = 0. \tag{III.2}$$

The pressure field $p(\boldsymbol{r},t)$ is determined by the condition that the flow remains incompressible:

$$\boldsymbol{\nabla}\cdot\boldsymbol{v} = 0. \tag{III.3}$$

B. Constitutive models

The viscoelastic stress $\boldsymbol{\Sigma}$ is specified by a constitutive model for the fluid in question. In this work we consider six widely used constitutive models. These are set out in Appendix A, along with values of any model parameters used in our numerical studies. While inevitably differing in their detailed form, all of them have the same general structure, which we now outline.

The viscoelastic stress

$$\boldsymbol{\Sigma} = G\boldsymbol{S}(\boldsymbol{W},\lambda,Q,\cdots) \tag{III.4}$$

is the product of a constant modulus G and a dimensionless tensorial function $\boldsymbol{S}$ of a microstructural conformation tensor $\boldsymbol{W}$, together with any other microscopic

variables relevant to the fluid under consideration. (We list these here simply as $\lambda, Q, \cdots$. For further details, see Appendix A.) For a polymeric (or wormlike micellar) fluid, the conformation tensor $\boldsymbol{W}$ could encode the ensemble average dyad of the end-to-end vector of a chain or subchain, depending on the level of description. For an emulsion or foam, it could encode the ensemble average dyad of the interfacial normals. The dynamics of the conformation tensor is then specified by a differential equation of the general form

$$\partial_t \boldsymbol{W} + \boldsymbol{v}.\nabla \boldsymbol{W} = \boldsymbol{f}(\nabla \boldsymbol{v}, \boldsymbol{W}, \lambda, Q \cdots), \qquad \text{(III.5)}$$

with counterpart scalar equations for the dynamics of $\lambda, Q, \cdots$, of the same differential form.

The governing equations of the six constitutive models studied in this work, all of which conform to this general structure, are set out in Appendix A. Among the these models, the Oldroyd B [61] and FENE-CR [62] models provide phenomenological descriptions for the dynamics of the conformation tensor $\boldsymbol{W}$ in dilute polymer solutions (with no additional variables $\lambda, Q, \cdots$). The Giesekus model [61] is a generalisation of Oldroyd B, aimed at modelling more concentrated polymeric fluids.

For a microscopically motivated description of more concentrated solutions or melts of entangled linear polymers, we use the Rolie-Poly model[63]. This also recovers the reptation-reaction model [64] of wormlike micelles for a particular choice of model parameters. It is based on the tube theory of Doi and Edwards [65], whereby a polymer chain (or wormlike micelle) is dynamically restricted by a confining tube of topological entanglements with the surrounding chains. The chain then refreshes its configuration by a process of 1D curvilinear diffusion along the tube contour, known as reptation. Later added to this basic description were the additional dynamical processes of chain stretch relaxation and convective constraint release [66–68] (CCR), in which the relaxation of the stretch of a test chain has the effect of also relaxing entanglement points, thereby facilitating the relaxation of tube orientation. The Rolie-Poly model [63] incorporates these three dynamical process into a differential constitutive equation for the dynamics of $\boldsymbol{W}$, as set out in Appendix A.

For a microscopically motivated description of entangled long-chain branched polymers we use the Pom-pom model [69, 70]. Here the presence of polymeric arms branching off each end of a polymer molecule's main backbone inhibits the reptation of that backbone and promotes its stretching between the branch-points. The Pom-pom model specifies dynamics of the conformation $\boldsymbol{W}$ of the backbone, and of the degree of backbone stretch, λ.

Finally we consider a phenomenological fluidity model of a broad class of disordered soft 'glassy' materials (foams, dense emulsions, colloids, microgels, *etc.*) [30–32]. Common to all these are the features of structural disorder (in a dense packing of emulsion droplets, for example) and metastability (with the large energy barriers involved in stretching soap films inhibiting rearrangements of the droplets). These glassy features give rise to rheological ageing, in which a sample becomes progressively more solid-like as a function of the time elapsed since it was prepared. The sustained application of flow however halts ageing and rejuvenates the sample to a steady state with an effective age set by the inverse flow rate. The flow curve displays a yield stress in the limit of slow flow. As outlined in Appendix A, our fluidity model specifies the dynamics of a tensor $\boldsymbol{W}$ characterising the conformation of the droplet interfaces, and of the total interfacial area Q. Also specified is an evolution equation for the ageing stress relaxation time τ. We have also checked that our results for the fluidity model, presented below, also hold within the more sophisticated soft glassy rheology model [31, 32, 49].

C. Units and parameter values.

Throughout we adopt units of length in which the initial length of the filament $L(0) = 1$, and units of stress in which the viscoelastic modulus $G = 1$. We use units of time in which the intrinsic relaxation timescale of any constitutive model is equal to unity. Accordingly, for the Oldroyd B, Giesekus and FENE-CR models we set $\tau = 1$. For the Rolie-Poly model we set $\tau_d = 1$. For the Pom-pom model we set $\tau_b = 1$. For the fluidity model of soft glasses we set the microscopic time $\tau_0 = 1$. (This model's actual stress relaxation time τ becomes highly separated from τ_0 during ageing.) The definition of these timescales can be found in Appendix A. Values for the other model parameters, in these units, are listed in table I of Appendix A.

D. Initial conditions, flow geometry and protocol.

We consider a sample of material that at some initial time $t = 0$ is in the shape of an undeformed uniform cylindrical filament of length $L(0)$ and cross sectional area $A(0)$, with an isotropic conformation tensor $\boldsymbol{W}(0) = \boldsymbol{I}$. Initial conditions for any additional variables $\lambda, Q, \cdots$ are prescribed in Appendix A. For all times $t > 0$ the filament is then subject to a constant applied Hencky strain rate $\bar{\dot{\epsilon}}$, such that its length increases as $L(t) = L(0)\exp(\bar{\dot{\epsilon}}t)$. The overbar signifies that $\bar{\dot{\epsilon}}$ is the strain rate experienced by the sample as a whole, globally averaged along its full length. Once necking arises, the deformation rate will locally vary along the filament's length z such that the Hencky strain rate $\dot{\epsilon} = \dot{\epsilon}(z, t)$, with the average $\bar{\dot{\epsilon}}$ of this function along z remaining constant in time.

E. Slender filament approximation

We adopt a slender filament approximation [39, 71, 72], in which the wavelengths of any variations that develop

in cross sectional area along the filament's length are assumed large compared to the filament's radius, and the flow variables are averaged across the filament's cross section at any location z along it. Relevant dynamical variables are then the cross sectional area $A(z,t)$, the area averaged fluid velocity in the z direction $V(z,t)$, and the extension rate $\dot{\epsilon}(z,t) = \partial_z V$. For clarity we drop the "+" superscript, usually used in Journal of Rheology to denote time-dependence in the extensional stress, from $\sigma_{\rm E}^{+}$ in the equations that follow.

The mass balance equation (III.3) is then written

$$\partial_t A + V\partial_z A = -\dot{\varepsilon}A, \tag{III.6}$$

and the force balance condition (III.2)

$$0 = \partial_z F, \tag{III.7}$$

in which the tensile force

$$F(t) = A(z,t)\sigma_{\rm E}(z,t), \tag{III.8}$$

and the total tensile stress

$$\sigma_{\rm E} = G\left(S_{zz} - S_{xx}\right) + 3\eta\dot{\varepsilon}. \tag{III.9}$$

As before, $\boldsymbol{S} = \boldsymbol{S}(\boldsymbol{W}, \lambda, Q, \cdots)$. The evolution equation for the confirmation tensor is now written as

$$\partial_t \boldsymbol{W}(z,t) + V\partial_z \boldsymbol{W} = \boldsymbol{f}(\dot{\epsilon}, \boldsymbol{W}, \lambda, Q, \cdots), \tag{III.10}$$

with counterpart scalar differential equations for the dynamics of $\lambda, Q, \cdots$.

F. Transformation to co-extending frame

In the constant Hencky strain rate experiment of interest here, the length of the filament increases exponentially in time as $L(t) = L(0)\exp(\bar{\dot{\epsilon}}t)$, and the area decreases (overall) as $A(t) = A(0)\exp(-\bar{\dot{\epsilon}}t)$ (subject to local variations due to necking). This makes it convenient to make a transformation to the coextending, cothinning frame. Accordingly we define new variables of length u, velocity v and area a:

$$\begin{aligned} u &= z\exp(-\bar{\dot{\epsilon}}t), \\ v(u,t) &= V(z,t)\exp(-\bar{\dot{\epsilon}}t), \\ a(u,t) &= A(z,t)\exp(\bar{\dot{\epsilon}}t). \end{aligned} \tag{III.11}$$

The differential operators then transform as

$$\partial_z \longrightarrow \exp(-\bar{\dot{\epsilon}}t)\partial_u, \tag{III.12}$$

$$\partial_t \longrightarrow \partial_t - \bar{\dot{\epsilon}}u\partial_u, \tag{III.13}$$

giving the transformed equations of mass balance

$$\partial_t a + (v - \bar{\dot{\epsilon}}u)\partial_u a = -(\dot{\epsilon} - \bar{\dot{\epsilon}})a, \tag{III.14}$$

and force balance

$$0 = \partial_u \tilde{F}, \tag{III.15}$$

where the transformed tensile force

$$\tilde{F}(t) = F(t)\exp(\bar{\dot{\epsilon}}t) = a(u,t)\sigma_{\rm E}(u,t). \tag{III.16}$$

The tensile stress $\sigma_{\rm E}^{+}$ is given as in III.9 above, with $\boldsymbol{S} = \boldsymbol{S}(\boldsymbol{W}, \lambda, Q, \cdots)$ as before. The transformed evolution equation for the conformation tensor is written as

$$\partial_t \boldsymbol{W} + (v - \bar{\dot{\epsilon}}u)\partial_u \boldsymbol{W} = \boldsymbol{f}(\dot{\epsilon}, \boldsymbol{W}, \lambda, Q, \cdots), \tag{III.17}$$

with counterpart scalar differential equations for any additional variables $\lambda, Q, \cdots$.

G. Simplified scalar model

So far, we have outlined the full tensorial constitutive models to be used in our numerical calculations, within a slender filament approximation. We shall also perform analytical calculations within a simplified scalar model that considers only the (assumed) dominant component $Z = W_{zz}$ of microstructural deformation that develops in a filament stretching experiment, also at the level of slender filament. Conditions of mass balance and force balance remain as in Eqns. III.14 to III.16 above. We then write the tensile stress simply as

$$\sigma_{\rm E} = GZ + \eta\dot{\epsilon}, \tag{III.18}$$

with the dynamics of Z specified as

$$\partial_t Z + V\partial_z Z = \dot{\epsilon}f(Z) - \frac{1}{\tau}g(Z), \tag{III.19}$$

with separate loading and relaxation dynamics characterised by the functions f and g respectively. For notational simplicity, in this scalar model, we have also absorbed a factor 3 into the solvent viscosity η.

Writing the model in this highly generalised form, without specifying any particular functional forms for the loading and relaxation dynamics $f(Z)$ and $g(Z)$, will enable us to derive criteria for the onset of necking that are reportable simply in terms of characteristic signatures in the shapes of the material response functions (tensile stress, *etc.*) as a function of the time (or accumulated strain) since the inception of the flow.

H. Boundary conditions

In our linear stability calculations we assume periodic boundary conditions between the two ends of the filament, thereby implicitly taking the filament to correspond to a torus being stretched. We performed our nonlinear numerical simulations for two different sets of boundary conditions in turn: first, we adopted the periodic boundary conditions just discussed; and second, we used an approximate mimic of the no-slip boundary condition between the fluid and the endplates. (The full

flow field near the plates cannot however be captured at the level of this slender filament calculation.)

The second of these conditions is discussed in detail in Sec. VII. As we shall demonstrate, it automatically provides some heterogeneity that seeds the formation of a neck in the sample. For the nonlinear simulations performed with the periodic boundary we instead seeded the instability by adding a small initial perturbation to the area profile such that $a(u, t = 0) = a(0) + \delta a_0 \cos(2\pi u)$ with $\delta a_0 \ll 1$. In fact we found the necking dynamics predicted with these two boundary conditions to be essentially the same, so shall present the results of our nonlinear simulations only with the second condition, mimicking no-slip.

IV. LINEAR STABILITY ANALYSIS: GENERAL PROCEDURE

We now outline in general terms the procedure of performing a linear stability analysis for the onset of necking. We start by considering a homogeneous "base state" corresponding to a filament that remains in a uniform cylindrical shape as it is stretched out, with the flow variables homogeneous along it. To this base state are then added small amplitude perturbations that are heterogeneous along the filament's length, corresponding to the precursor of a neck. Expanding the governing equations to first order in the amplitude of these perturbations gives linearised equations for the dynamics of the perturbations. Integrating these in time, and/or examining the eigenvalues of the matrix that governs the linear equations, then determines whether, and at what time during the filament stretching process the perturbations grow and thereby take the system towards a necked state, or whether they decay to leave a uniform filament.

A. Homogeneous base state

We consider first a uniform "base state", labelled with a subscript 0, corresponding to a filament that remains a uniform cylinder as it is stretched out, with all flow variables homogeneous along it. In this state the strain rate $\dot{\epsilon}(u, t) = \dot{\epsilon}_0 = \bar{\dot{\epsilon}}$, the transformed velocity $v(u, t) = v_0 = u\bar{\dot{\epsilon}}$ and the transformed area $a(u, t) = a_0 = A(0)$. (In the laboratory frame, the area thins as $A(t) = A(0)\exp(-\bar{\dot{\epsilon}}t)$.) The viscoelastic variables, for which no frame transformation is needed, follow as homogeneous solutions $\boldsymbol{W}_0(t), \lambda_0(t), Q_0(t), \cdots$ of their respective equations of motion (III.10 and its counterparts for $\lambda, Q, \cdots$) for times $t > 0$, subject to the initial condition of the filament having been undeformed priori to time $t = 0$. The time-dependent tensile stress

$$\sigma_{\mathrm{E}0}(\dot{\epsilon}, t) = G\left(S_{zz0} - S_{xx0}\right) + 3\eta\bar{\dot{\epsilon}}, \tag{IV.1}$$

with

$$\boldsymbol{S}_0 = \boldsymbol{S}(\boldsymbol{W}_0(t), \lambda_0(t), Q_0(t), \cdots). \tag{IV.2}$$

If the tensile stress attains a steady state in the limit of long times $t \to \infty$ after the inception of the flow, once many strain units $\bar{\epsilon} = \bar{\dot{\epsilon}}t$ have been applied, the steady state relation $\sigma_{\mathrm{E}0}(\bar{\dot{\epsilon}})$ defines the material's homogeneous extensional constitutive curve. The constitutive curves of the six models considered in this work are shown in Fig. 2. We shall return in the results sections below to describe the shapes of these curves in more detail, in particular discussing any features that pertain to necking.

The time-evolution $\sigma^{+}_{\mathrm{E}0}(t)$ of the homogeneous stress signal towards this steady state constitutive curve is shown at several different imposed strain rates for the Giesekus and Rolie-Poly models in the left panels of Fig. 1. The corresponding (untransformed) tensile force $F(t) = \sigma^{+}_{\mathrm{E}}(t)A(t)$ is shown in the right panels of the same figure. The force initially increases, due to the rising stress, then later decreases, due to the declining cross sectional area.

Without loss of generality we are at liberty to set the initial cylinder area $A(0) = a_0 = 1$. Note that this is in addition to having set the initial cylinder length $L(0) = 1$ in our choice of units above. It is important to realise, however, that we are not restricting ourselves to situations in which the initial area and length are constrained relative to each other in any particular way. Any information about the relative values of the cylinder's area and length has simply been lost as a consequence of making the slender filament approximation [50, 72].

B. Heterogeneous perturbations

So far we have discussed a calculation in which the filament is assumed to remain perfectly uniform as it is stretched out, with all the flow variables homogeneous along it. In the language of hydrodynamic stability theory, this gives a "base state" $(\bar{\dot{\epsilon}}, a_0, \boldsymbol{W}_0(t), \lambda_0(t), Q_0(t), \cdots)$. In contrast to conventional stability calculations, however, this base state is time-dependent, because of the time-evolution of the viscoelastic conformation variables following the onset of the applied flow, giving rise to the time-evolving tensile stress signals in Fig. 1 (left panels). Eventually, after several strain units, the base state will attain a steady state with a tensile stress on the homogeneous constitutive curve. As the calculations that follow will show, however, the sample will in general neck significantly before the system has a chance to attain a state of homogeneous flow on that constitutive curve.

To study how this necking arises, we now add to the homogeneous base state small amplitude heterogeneous perturbations, decomposed into Fourier modes with wavevector q that is reciprocal to the space vari-

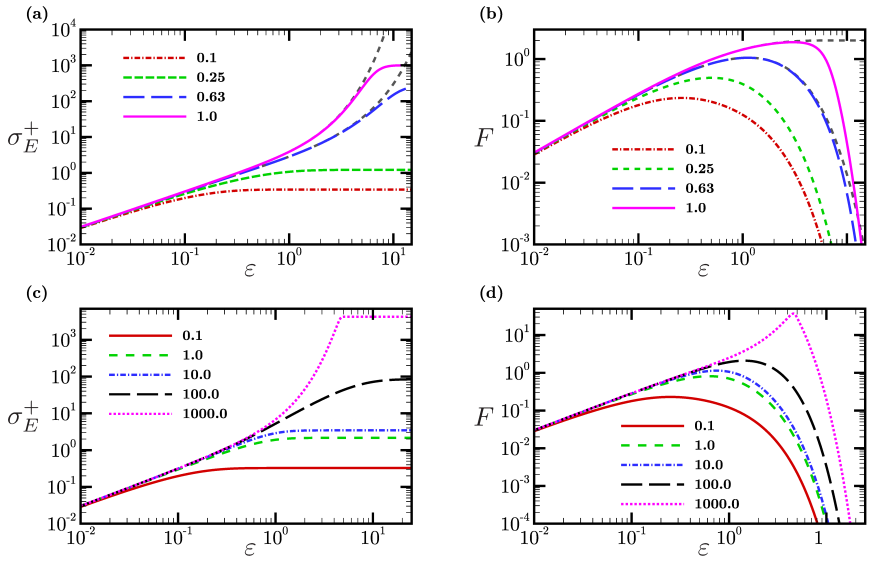

FIG. 1. Transient evolution of the stress $\sigma_{\rm E}^+$ (left) and the force F (right) for the Giesekus model (top) and the finite-stretch Rolie-Poly model (bottom), within a calculation that artificially constrains the flow to remain homogeneous. The key shows the strain rate for each data set. The counterpart steady-state homogeneous constitutive curves $\sigma_{\rm E}(\dot\epsilon, t\to\infty)$ can be seen in figure 2. Parameter values for each model are given in appendix A, table I. The grey dashed curves in the Giesekus (top) figures show for comparison results for the Oldroyd B model, to which the Giesekus model reduces in the limit $\alpha\to 0$.

able u along the filament's transformed length:

$$\begin{pmatrix} \dot\epsilon(u,t) \\ a(u,t) \\ \boldsymbol{W}(u,t) \\ \lambda(u,t) \\ Q(u,t) \\ \vdots \end{pmatrix} = \begin{pmatrix} \bar{\dot\epsilon} \\ a_0 \\ \boldsymbol{W}_0(t) \\ \lambda_0(t) \\ Q_0(t) \\ \vdots \end{pmatrix} + \sum_q \begin{pmatrix} \delta\dot\epsilon(t) \\ \delta a(t) \\ \delta\boldsymbol{W}(t) \\ \delta\lambda(t) \\ \delta Q(t) \\ \vdots \end{pmatrix}_q \exp(iqu). \tag{IV.3}$$

Note that the area perturbations $\delta a(t)$ obey $\delta a(t)/a_0 = \delta A(t)/A(t)$ where a_0 is constant. They thereby give a measure, at any time t, of the fractional variations in cross sectional area along the filament's length, compared to the length-averaged cross sectional area at that time. They therefore indicate the degree to which the filament has necked at that time.

We then substitute this expression (IV.3) into the governing equations (III.14) to (III.17), expand in successive powers of the amplitude of the perturbations, and retain only terms of first order in this amplitude. This gives linearised equations for the dynamics of the perturbations:

$$\partial_t \begin{pmatrix} \delta\dot\epsilon(t) \\ \delta a(t) \\ \delta\boldsymbol{W}(t) \\ \delta\lambda(t) \\ \delta Q(t) \\ \vdots \end{pmatrix}_q = \boldsymbol{M}(t)\cdot \begin{pmatrix} \delta\dot\epsilon(t) \\ \delta a(t) \\ \delta\boldsymbol{W}(t) \\ \delta\lambda(t) \\ \delta Q(t) \\ \vdots \end{pmatrix}_q , \tag{IV.4}$$

in which it is important to note that the stability matrix $\boldsymbol{M}(t)$ has inherited the time-dependence of the base state $(\bar{\dot\epsilon}, a_0, \boldsymbol{W}_0(t), \lambda_0(t), Q_0(t), \cdots)$, upon which it depends.

We note that the stability matrix $\boldsymbol{M}(t)$ has however no dependence on the wavevector q. This stems from the fact that the governing equations (III.14) to (III.17) are spatially local, apart from the convective terms, which drop out at linear order in the above expansion. (Spatial dependence of $\boldsymbol{M}$ would however be restored at lengthscales shorter than those considered here by moving beyond our slender filament assumption, or by incorporating surface tension, or by including stress diffusion, which would cutoff any instability at short lengthscales.) In this way, all Fourier modes $\exp(iqu)$ are predicted to have the same dynamics. Which mode will dominate any necking stability in practice is therefore determined by which is initially seeded most strongly: whether by thermal noise, slight initial sample imperfection, or by geometrical features of the experimental device. In a filament stretching rheometer we expect the dominant seeding to arise from the no-slip condition that applies where sample ends meet the rheometer plates. As noted above, this constrains the area to remain constant at each of the sample ends as the sample is stretched out overall, thereby initiating a single neck in the middle of the filament. (It is this effect that is modelled in our nonlinear simulations by the boundary condition discussed at the start of Sec. VII.)

To determine whether in any filament stretching experiment the perturbations $\delta a(t)$ in the filament's cross sectional area will start to grow towards a necked state, and at what time during the run they first start to do so, these linearised equations must be integrated in time. If the stability matrix $\boldsymbol{M}$ were time-independent, it would be trivial to establish that δa would grow if at least one eigenvalue of $\boldsymbol{M}$ had positive real part. The time-

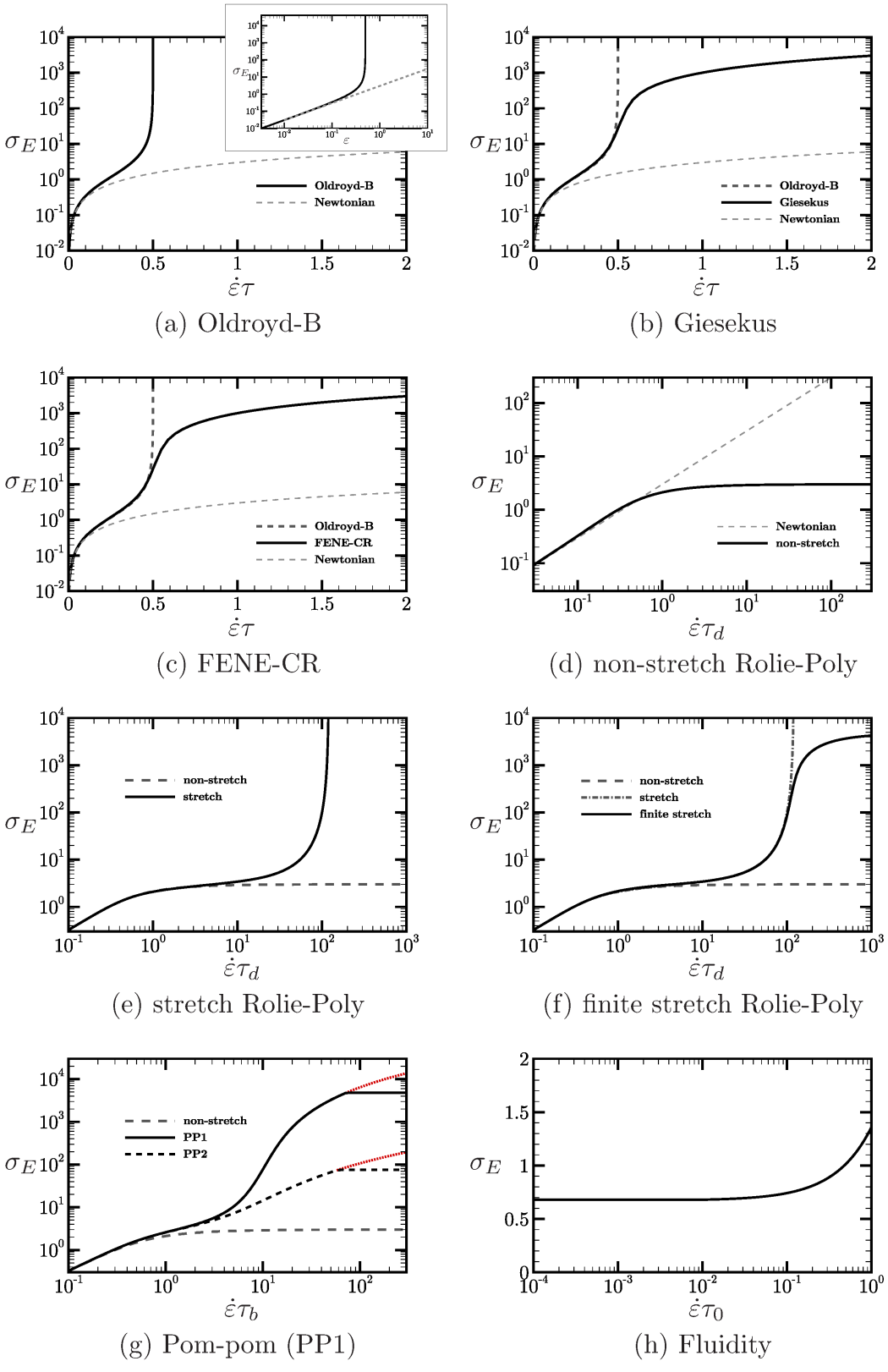

FIG. 2. Stationary homogeneous extensional constitutive curves of the models to be studied, for the model parameters values specified in App. A, table I. The apparent negative curvature at low strain rates in (a), (b) and (c) is a consequence of the log-linear scale. The more familiar log-log scale is shown as an inset for the Oldroyd B model in (a). In (g) the black curves show the constitutive curves for the form of the Pom-pom model in which the backbone stretch has a hard cutoff. The red-dotted lines show the equivalent curves for a form of the model in which that cutoff is removed. See the discussion at the end of Sec. VII B.

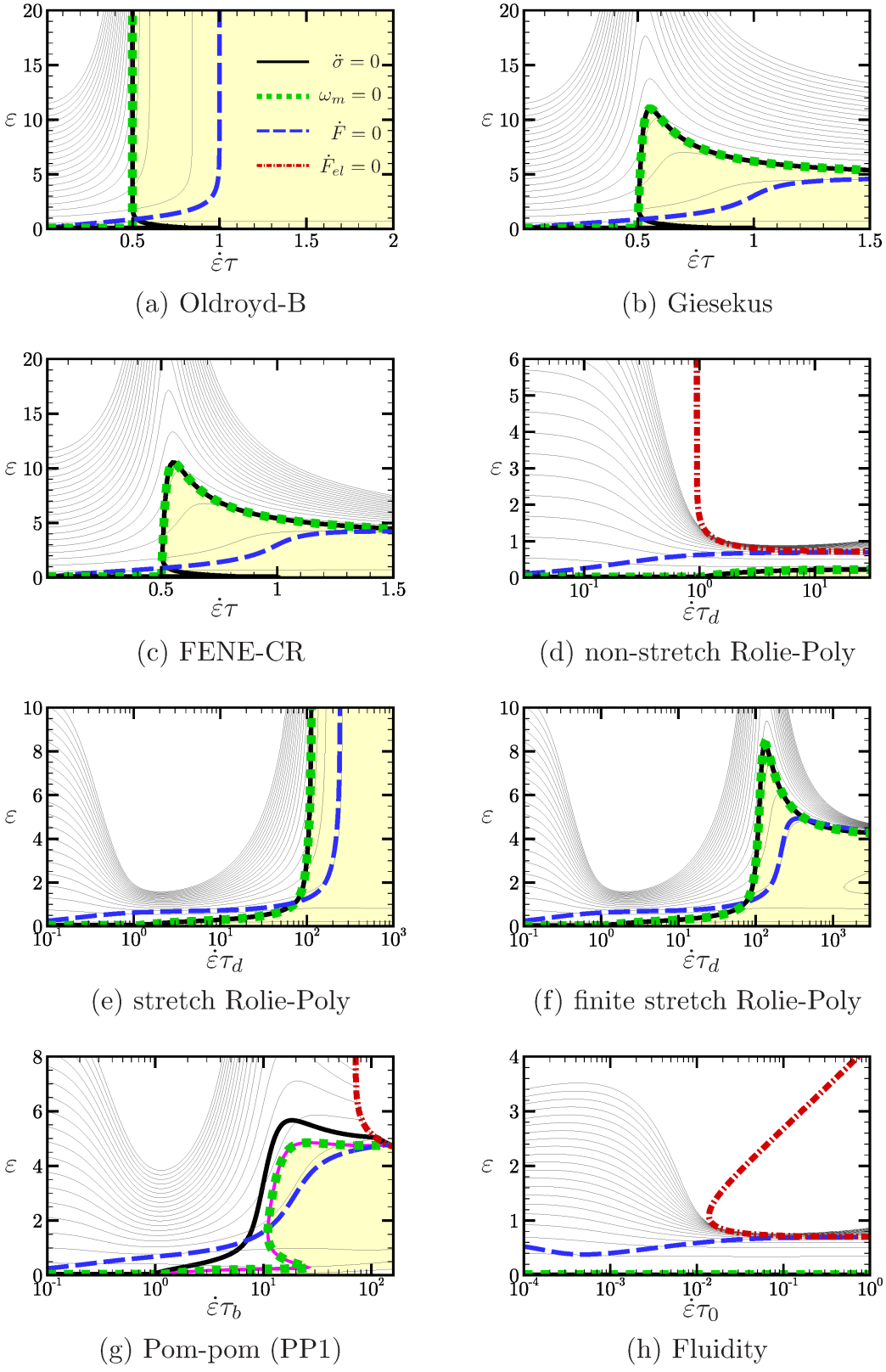

(a) Oldroyd-B (b) Giesekus

(c) FENE-CR (d) non-stretch Rolie-Poly

(e) stretch Rolie-Poly (f) finite stretch Rolie-Poly

(g) Pom-pom (PP1) (h) Fluidity

FIG. 3. Numerical results for the linearised necking dynamics within six tensorial constitutive models. (Results for the Rolie-Poly model are shown separately with chain stretch disallowed (d); with chain stretched allowed and unrestricted (e); and with chain stretched allowed but restricted to be finite (f).) The thin black lines show contours of constant area perturbations $\delta a/\delta a_0 = 10^{n/4}$, with $n = 1 \cdots 20$ in curves from bottom to top, representing the growing degree of necking at increasing strain ϵ upwards in any filament stretching experiment at fixed $\dot{\epsilon}$. The green dotted lines shows the strain at which the largest eigenvalue becomes positive, in increasing strain ϵ upwards during stretching at fixed $\dot{\epsilon}$. (The overhang in the Pom-pom model gives stability-instability-stability-instability in the range of strain rates $10 < \dot{\epsilon}\tau < 30$.) Accordingly, the beige shaded area shows the window of strains over which the filament is stable against necking. The thick black solid line shows the strain at which the stress curvature criterion predicts the onset of necking, in increasing ϵ at fixed $\dot{\epsilon}$. The red dot-dashed line shows the strain at which the "elastic Considère " mode becomes unstable. The blue long-dashed line shows the strain at which the original Considère criterion would predict the onset of necking.

dependence of $\boldsymbol{M}$ clearly complicates this, although a good indication of whether the area fluctuations δa will be growing at any time during a run is given by whether (at least) one of the time-dependent eigenvalues of $\boldsymbol{M}$ has a positive real part at that time. However the concept of a time-dependent eigenvalue is clearly delicate. In our numerical simulations of the six constitutive models in Sec. VI below, therefore, we both directly integrate the linearised equations *and* report the more indirect measure given by the sign of the real part of the time-dependent eigenvalue of $\boldsymbol{M}$ with the largest real part. Pleasingly, we find good agreement between the regime of strongly growing area fluctuations δa, and of a positive eigenvalue of $\boldsymbol{M}$.

The aim of the next section is to analytically derive fluid-universal (model-independent) criteria for the time at which this necking instability first sets in during any filament stretching run, which we can then compare with our numerical simulations of the six constitutive models.

V. CRITERIA FOR NECKING

Having outlined the procedure of a linear stability analysis in general terms, we now perform this calculation analytically in the particular case of the simplified scalar model introduced in Sec. III G. Our goal in doing so is to derive criteria for the onset of necking that can be reported in terms of characteristic signatures in the shapes of the material response functions (tensile stress σ_{E}^{+}, *etc.*) as a function of the time (or accumulated strain) since the inception of the flow. Recall that the original Considère criterion would predict the onset of necking to coincide with the characteristic signature $\partial_\epsilon F < 0$ in the functional form of the tensile force F as a function of the accumulated strain ϵ. As noted above, however, there is no reason a priori to expect this criterion for necking in solids to apply in complex fluids with a finite stress relaxation timescale τ.

We start by recollecting for convenience the governing equations. The condition of mass balance gives

$$\partial_t a + (v - \bar{\dot{\epsilon}}u)\partial_u a = -(\dot{\epsilon} - \bar{\dot{\epsilon}})a. \tag{V.1}$$

The condition of force balance for the transformed force $\tilde{F}(t) = F(t)\exp(\bar{\dot{\epsilon}}t)$ gives

$$0 = \partial_u \tilde{F} = \partial_u(a\sigma_{\mathrm{E}}), \tag{V.2}$$

where the tensile stress

$$\sigma_{\mathrm{E}} = GZ + \eta\dot{\epsilon}. \tag{V.3}$$

The scalar conformation variable evolves as

$$\partial_t Z + (v - \bar{\dot{\epsilon}}u)\partial_u Z = \dot{\epsilon} f(Z) - \frac{1}{\tau} g(Z), \tag{V.4}$$

We intentionally leave unspecified the forms of the loading and relaxation functions $f(Z)$ and $g(Z)$ in order that the criteria we derive are as fluid-universal as possible, independent of particular constitutive choices.

Following the procedure outlined above, we consider a uniform base state $\bar{\dot{\epsilon}}, a_0, Z_0(t)$, in which the viscoelastic conformation variable $Z_0(t)$ evolves as a function of the time t since the inception of the flow in a manner prescribed by Eqn. V.4, solved within the assumption of homogeneous flow, $\partial_u Z_0 = 0$. The tensile stress $\sigma_{\mathrm{E}0}^{+}(t) = GZ_0(t) + \eta\bar{\dot{\epsilon}}$ accordingly evolves (in the absence of pathological choices for the loading and relaxation functions f and g) towards its eventual steady state on the homogeneous constitutive curve at the given applied strain rate $\bar{\dot{\epsilon}}$. The corresponding tensile force $F_0(t) = \sigma_{\mathrm{E}0}^{+}(t)A_0(t)$ initially increases as a result of the rising stress, then decreases due to the declining filament area $A_0(t) = A(0)\exp(-\bar{\dot{\epsilon}}t)$.

To this uniform, time-evolving base state we now add small amplitude heterogeneous perturbations, which are the precursor of any neck:

$$\begin{pmatrix} \dot{\epsilon}(u,t) \\ a(u,t) \\ Z(u,t) \end{pmatrix} = \begin{pmatrix} \bar{\dot{\epsilon}} \\ a_0 \\ Z_0(t) \end{pmatrix} + \sum_q \begin{pmatrix} \delta\dot{\epsilon}(t) \\ \delta a(t) \\ \delta Z(t) \end{pmatrix}_q \exp(iqu). \tag{V.5}$$

(We have kept the q subscript here as a reminder that we consider perturbations on all spatial lengthscales. However the reader should recall the discussion in the previous section, noting that the stability matrix is actually $q-$indpendent and that instead the dominant mode will be the one seeded most strongly by endplate effects, leading to a single neck mid-filament.) Substituting (**??**) into the governing equations (V.1) to (V.4), expanding in powers of the amplitude of the perturbations, and retaining only terms of first order in that amplitude, gives a set of linearised equations for the dynamics of the perturbations.

The linearised mass balance equation is

$$\partial_t \delta a_q = -\delta\dot{\epsilon}_q. \tag{V.6}$$

The linearised force balance equation is

$$0 = \sigma_{\mathrm{E}}\delta a_q + G\delta Z_q + \eta\delta\dot{\epsilon}_q, \tag{V.7}$$

and the linearised viscoelastic constitutive dynamics

$$\partial_t \delta Z_q = \delta\dot{\epsilon}_q f(Z_0) + C\delta Z_q \tag{V.8}$$

in which

$$C = \dot{\epsilon} f'(Z_0) - \frac{1}{\tau} g'(Z_0). \tag{V.9}$$

Here and throughout we use a prime to denote differentiation with respect to a function's own argument. Eliminating $\delta\dot{\epsilon}_q$, which is instantaneously slaved to the other variables by the condition of force balance in creeping flow, gives the two-dimensional linearised equation set:

$$\partial_t \begin{pmatrix} \delta a(t) \\ \\ \delta Z(t) \end{pmatrix}_q = \boldsymbol{M}(t) \cdot \begin{pmatrix} \delta a(t) \\ \\ \delta Z(t) \end{pmatrix}_q . \tag{V.10}$$

This is governed by the stability matrix

$$\boldsymbol{M}(t) = \begin{pmatrix} \dfrac{\sigma_{\mathrm{E}0}}{\eta} & \dfrac{G}{\eta} \\ \dfrac{-f(Z_0)\sigma_{\mathrm{E}0}}{\eta} & -\dfrac{f(Z_0)G}{\eta} + C \end{pmatrix}. \quad \text{(V.11)}$$

This depends on time via the evolving viscoelastic conformation variable $Z_0(t)$ in the base state, until that base state settles to a steady state with the tensile stress on the stationary homogeneous constitutive curve. As we shall see below, however, the sample in general necks significantly before any such stationary homogeneous state can be attained.

Denoting the trace and determinant of $\boldsymbol{M}$ by T and Δ respectively, we have

$$T = \frac{1}{\eta}(\sigma_{\mathrm{E}0} - fG) + O(1), \quad \text{(V.12)}$$

and

$$\Delta = \frac{\sigma_{\mathrm{E}0}C}{\eta}. \quad \text{(V.13)}$$

In what follows we assume the solvent viscosity η small compared to the scale of the viscoelastic viscosities, and accordingly ignore the $O(1)$ term in T.

It is possible to show that these expressions for T and Δ can be cast in terms of more physically meaningful properties of the underlying base state as follows:

$$T = -\frac{1}{A(0)\eta}\partial_\epsilon F_{\mathrm{elastic}}, \quad \text{(V.14)}$$

and

$$\Delta = \frac{\sigma_{\mathrm{E}0}}{\eta}\frac{\ddot{\sigma}_{\mathrm{E}0}}{\dot{\sigma}_{\mathrm{E}0}}, \quad \text{(V.15)}$$

where dot denotes time differentiation. Note that the derivative $\partial_\epsilon F_{\mathrm{elastic}}$ of the base state's tensile force with respect to strain ϵ in Eqn. V.14 needs careful interpretation. It is defined by evolving the state up to some strain ϵ with the full model dynamics, including loading by flow as encoded by f and relaxation as encoded by g. In the next increment of strain $\epsilon \to \epsilon + \delta\epsilon$ over which the derivative is taken the relaxation term $g(Z)$ is then suppressed, with only the loading ('elastic') dynamics implemented. Necking in the elastic limit of viscoelastic models was also discussed in [35].

The time-dependent eigenvalues $\omega(t)$ of $\boldsymbol{M}$ follow as solutions of the quadratic

$$\omega^2 - T\omega + \Delta = 0. \quad \text{(V.16)}$$

By examining the conditions under which these can become positive (in the sense of having a positive real part) during the course of a filament stretching run, we find two different possible modes of instability to necking. The first gives instability in any regime where the determinant $\Delta < 0$, and accordingly where

$$\frac{\ddot{\sigma}_{\mathrm{E}}}{\dot{\sigma}_{\mathrm{E}}} < 0. \quad \text{(V.17)}$$

(We return below to justify the fact that we have just dropped the base state subscript, writing $\sigma_{\mathrm{E}0} \to \sigma_{\mathrm{E}}$.) In all the constitutive models considered in this work the tensile stress increases monotonically towards the constitutive curve (at least before significant necking occurs), $\dot{\sigma}_{\mathrm{E}} > 0$, and the criterion for the onset of necking instability is simply

$$\ddot{\sigma}_{\mathrm{E}} < 0. \qquad \textbf{"Stress curvature mode"} \quad \text{(V.18)}$$

Its eigenvalue has an amplitude set by the imposed strain rate $\dot{\bar{\epsilon}}$. Once this mode of instability sets in, therefore, it gives rise to an observable neck over the course of a few strain units. Note that in some experiments the stress signal has been observed to overshoot on its approach to the constitutive curve, giving $\dot{\sigma}_{\mathrm{E}} < 0$ after the overshoot [60]. The implications of this for necking will be considered in future work.

The second mode gives instability in any regime where the trace $T > 0$, and so where

$$\partial_\epsilon F_{\mathrm{elastic}} < 0. \quad \textbf{"Elastic Considère mode"} \quad \text{(V.19)}$$

Its eigenvalue has an amplitude $O(G/\eta)$, which is large for the small solvent viscosities relevant to the highly viscoelastic materials considered here. If this mode becomes unstable during any filament stretching run, it causes a neck to then develop very quickly compared to the rate of the imposed flow.

Note that we have dropped the base-state subscript "0" in writing (V.18) and (V.19). This is justified because the base-state properties contained in these expressions – in particular the stress curvature $\ddot{\sigma}_{\mathrm{E}}$ in (V.18) – also correspond to the full experimentally measured properties at least as long as the sample remains uniform, and therefore up to the point that significant necking occurs. Accordingly, the experimentally measured signals can be used in these expressions in order to predict the onset of necking.

The stress signal σ_{E}^+ in (V.18) is widely reported in the experimental literature. Whether the "elastic" derivative of the force $\partial_\epsilon F_{\mathrm{elastic}}$ in (V.19) has any easily measurable counterpart is an open question. In any case, it is crucial to note that the condition $\partial_\epsilon F_{\mathrm{elastic}} = 0$ does *not* correspond to the condition $\partial_\epsilon F = 0$. This new "elastic" Considère criterion is therefore *not* (in general) the same as the original Considère criterion, which predicts necking instability when $\partial_\epsilon F < 0$. Indeed our numerical results below will show that the two conditions predict the onset of instability at different strains over most of the range of imposed strain rates $\dot{\epsilon}$. They do, however coincide as $\dot{\epsilon}\tau \to \infty$. This is to be expected, because in this limit a fluid's relaxation dynamics, as encoded by

g/τ here, become unimportant compared to the loading by flow, as encoded by $\dot{\epsilon}f$.

Note that we chose to express the stress curvature criterion in terms of time derivatives of the stress, and the elastic Considère criterion in terms of a strain (elastic) derivative of the force. However both criteria can equally be expressed in either time or strain derivatives, because $\partial_t = \dot{\epsilon}\partial_\epsilon$ for the constant $\dot{\epsilon}$ protocol of interest here. We chose our notation simply because the stress curvature criterion corresponds to a rather gradual, liquid-like mode of instability, for which time seems the more the natural independent variable. In contrast, the elastic Considère criterion pertains to a solid-like mode, for which strain seems more the natural variable.

Because these criteria for necking have been derived within a highly generalised constitutive model, independent of any particular constitutive choices for the functions f and g, we suggest that they should apply rather widely among materials that show a basic competition between elastic loading and viscoelastic (or plastic) relaxation. Pleasingly, our numerical results in Sec. VI will show that they hold either exactly or to a good level of approximation in all of the six tensorial constitutive models considered in this work.

Indeed, making the concrete choices $f = 3 + 2Z - \beta Z^2$ and $g = Z + \alpha Z^2$ for the loading and relaxation functions in this scalar model gives an excellent approximation to the necking predictions of the full tensorial Oldroyd B model ($\alpha = \beta = 0$), the Giesekus and FENE-CR models ($\alpha \neq 0, \beta = 0$) and the Rolie-Poly model without chain stretch ($\alpha = 0, \beta \neq 0$). We verified this by comparing numerical results for the scalar model with these parameter choices with their counterparts in the full tensorial models, finding excellent agreement (Appendix A 7).

VI. NUMERICAL RESULTS: LINEAR STABILITY

Having derived criteria for the onset of necking, we now present numerical results to demonstrate their validity within six widely used tensorial constitutive models. See Fig. 3. Each panel of this figure contains results presented in the plane $(\epsilon, \dot{\epsilon})$ of strain and strain rate (with the latter expressed in units of the characteristic relaxation time in any model). Any vertical line from bottom to top in this plane tracks a single filament stretching run performed at constant strain rate $\dot{\epsilon}$, with the strain ϵ increasing upwards in the plane as the filament is stretched out. (Note that in previous sections we used $\bar{\dot{\epsilon}}$ to denote the strain rate applied globally to the sample as a whole, and $\dot{\epsilon}(z,t)$ the strain rate that varies locally along the filament as the sample necks. In the results sections that follow, we often use $\dot{\epsilon}$ to denote the globally applied strain rate for notational convenience.)

The thin solid black lines show contours of constant area perturbation $\delta a(t)$. (Recall the note after Eqn IV.3 regarding the definition of δa.) Each successive contour crossing (as ϵ increases upwards at fixed $\dot{\epsilon}$) corresponding to an increase of factor $10^{1/4}$ in the area perturbation, such that the nth contour represents a degree of necking $\delta a/\delta a_0 = 10^{n/4}$, where δa_0 is the initial small seeding provided at the start of the run. The more densely clustered the contour lines vertically at any fixed $\dot{\epsilon}$, therefore, the faster necking occurs in a filament stretching run at that strain rate. We have shown only the first 20 contour lines, assuming that the sample will have failed altogether by this time. Indeed, although the absolute necking amplitudes associated with these contours are arbitrary at the level of this linear analysis, a good indication of the dependence of the strain at which the sample is likely to finally fail on the imposed strain rate is given by focusing on one representative contour.

Also included in each panel is a green dotted line showing the strain ϵ at which the largest eigenvalue ω_m first becomes positive (in the sense of having a positive real part) in any filament stretching run at a given strain rate $\dot{\epsilon}$, signifying the onset of instability to necking. (The slight overhang in the Pom-pom model gives stability-instability-stability-instability in the range of strain rates $10 < \dot{\epsilon}\tau < 30$.) Accordingly, the beige shading shows the window of strains in which the sample is stable against necking at any given imposed strain rate. As can be seen, the onset of a positive eigenvalue agrees convincingly with the onset of strong exponential growth in necking depicted by the contour lines. (Some transient growth is seen before the eigenvalue becomes positive, but of an amplitude unlikely to be seen experimentally.)

The thick black solid line in each panel depicts the strain at which the stress curvature criterion predicts the onset of necking, as the strain increases in any filament stretching run at fixed $\dot{\epsilon}$. For strains below this line, the stress is an upwardly curving function of time (or accumulated strain). For strains above it, the stress curves downward in time as it tends finally towards the constitutive curve. (Recall Fig. 1.) As can be seen, this stress curvature criterion exactly predicts the onset of necking (*i.e.,* the change in sign of the eigenvalue) in the Oldroyd B, Giesekus, FENE-CR, and Rolie-Poly models, apart from a slight discrepancy at small strains [73]. It also performs qualitatively well in the Pom-pom model, with some quantitative discrepancy [74]. In the fluidity model the curvature criterion is negative from the inception of flow for all strain rates.

In the Oldroyd B, Giesekus, FENE-CR and Rolie-Poly model (with chain stretch), the stress curvature mode of necking instability just discussed is the only one that arises. As noted above, it leads to relatively gentle necking with an eigenvalue of characteristic amplitude set by $\dot{\epsilon}$. In stark contrast, at high strain rates in the Roly-Poly model without chain stretch, and in the Pom-pom and fluidity models, the "elastic Considère " mode also arises. The strain at which it sets in is indicated by the red dot-dashed lines. Once active, it causes very fast necking, with an eigenvalue $O(G/\eta)$: the contours of δa then become almost too narrowly spaced to be separately

discerned on the strain scale of the plots in Fig. 3, and the sample fails catastrophically quickly.

This difference in severity between the stress curvature and elastic Considère modes leads to radically different necking dynamics at low and high strain rates in these three models (Figs. 3d,g,h). At low strain rates, necking occurs gradually via the stress curvature mode. At high strain rates the sample violently fails via the elastic Considère mode. However in any case where the elastic Considère mode does become unstable, it does so only after the stress curvature mode has already caused some necking. In this sense, it can be seen as a rapid amplifier of an already existing, but much gentler instability. (In the fluidity model a return to elastic-Considère stability is seen at larger strains at high strain rates, but this is of no relevance because the sample will have already entirely failed by that point.)

Having discussed the general features of the plots in Fig. 3, we now describe in more detail the necking dynamics of each constitutive model in turn, starting with the Oldroyd B model in panel a). Here the dominant contribution GW_{zz} to the tensile stress $\sigma_{\rm E}^{+}$ has a time-dependence of shape $1+\exp\left[(2\dot\epsilon-1/\tau)t\right]$. For imposed strain rates $\dot\epsilon<1/2\tau$, therefore, the stress curves downwards as a function of time, and a neck starts to form, right from the inception of the flow. In contrast, for imposed strain rates $\dot\epsilon>1/2\tau$ the stress signal curves upwards in time indefinitely. This is a result of the fact that the molecular dumbbells that this model describes can stretch out indefinitely with flow, consistent with the absence at these strain rates of a steady state in the constitutive curve of Fig. 2a). Although this well known 'extensional catastrophe' indefinitely stabilises the filament against necking, it is an unphysical feature of the Oldroyd B model. We note that the predictions of Fig. 3a) agree with earlier work in [39].

The FENE-CR and Giesekus models each contain nonlinearities that regularise this extensional catastrophe, cutting off the indefinite dumbbell stretching and restoring a finite stress even at strain rates $\dot\epsilon>1/2\tau$ in the constitutive curves of Fig. 2b,c). (Both models reduce back to Oldroyd B when those nonlinearities are removed.) The Giesekus model, for example, includes an additional term in the relaxation dynamics, $Z/\tau\to(Z+\alpha Z^2)/\tau$, with α small, recovering Oldroyd B when $\alpha=0$. These nonlinearities manifest themselves only once the dumbbells become strongly stretched, such that $\alpha Z=O(1)$. Because of this, for strain rates $\dot\epsilon<1/2\tau$ the dynamics of Giesekus and FENE-CR are essentially the same as Oldroyd B, with a downwardly curving stress $\sigma_{\rm E}^{+}(t)$ and instability to necking. Similarly at higher strain rates $\dot\epsilon>1/2\tau$, and for strains less than around $5-10$, before strong chain stretch arises, Giesekus and FENE-CR display an upwardly curving $\sigma_{\rm E}^{+}(t)$ and stability against necking, as in Oldroyd B. Compare panels b,c) and a) in Fig. 3.

In contrast, beyond a typical strain $5-10$ for strain rates $\dot\epsilon>1/2\tau$, the chain stretch becomes significant and the nonlinearities of Giesekus and FENE-CR become important, departing from the dynamics of Oldroyd B. In particular the chain stretch saturates, the upward curvature in the stress signal is halted, and the stress displays an inflexion point $\ddot\sigma_{\rm E}=0$, beyond which the stress curves downwards as a function of time (or accumulated strain) as it tends towards the constitutive curve (which it in general however will not reach before significant necking occurs). The filament then, indeed, becomes unstable to necking, as seen by the closely gathered contours beyond the green dotted line in Figs. 3b,c)

The three models discussed so far provide phenomenological descriptions of the rheology of polymer solutions. We now turn to the microscopically motivated Rolie-Poly (RP) model, which describes more concentrated solutions and melts of entangled linear polymers. It contains the basic dynamical processes of reptation, in which the orientation of a test chain relaxes on a timescale τ_d; chain stretch, which relaxes on a much faster timescales τ_s; and convective constraint release (CCR), in which the relaxation of chain stretch releases entanglement points and so also allows some relaxation of orientation.

Before describing the necking predictions of the RP model, we recall its extensional constitutive curves in Figs. 2d,e,f). Setting $\tau_s\to 0$ gives the non-stretching Rolie-Poly (nRP) model, for which the constitutive curve (Fig. 2d) has a regime of linear response at low strain rates, then a plateau for strain rates $\dot\epsilon>1/\tau_d$ where the chain orientation saturates. Restoring a finite τ_s gives the stretching Rolie-Poly (sRP). For strain rates $\dot\epsilon\ll 1/\tau_s$ its constitutive curve (Fig. 2e) is essentially the same as that of the nRP model, with minimal chain stretch. For $\dot\epsilon=O(1/\tau_s)$ and above, however, significant chain stretch develops and the stress correspondingly increases. Indeed in the raw form of the sRP model the stress diverges as $\dot\epsilon\to 1/\tau_s$, in direct counterpart to the stretch catastrophe of the Oldroyd B model. Including 'FENE' terms to give the finite-stretch Rolie-Poly (fsRP) model regularises this, as in moving from Oldroyd B to FENE-CR, eliminating the possibility of indefinite chain stretch and restoring a finite stress at all strain rates (Fig. 2f).

We now address the necking predictions of the Rolie-Poly model, starting with the version without chain stretch (the nRP model). See Fig. 3d. Here the stress curvature criterion predicts necking instability right from the inception of the flow for strain rates $\dot\epsilon<1/\tau_d$, and after a only a modest accumulated strain for $\dot\epsilon>1/\tau_d$. Furthermore, in this regime $\dot\epsilon>1/\tau_d$ the elastic Considère mode also sets in after an accumulated strain $\epsilon=O(1)$, causing violently fast necking once it does so. Just as in Oldroyd B the indefinite chain stretch and associated divergence in tensile stress indefinitely stabilised a filament against necking, so conversely the absence of chain stretch and the associated saturation in the stress with increasing strain rate cause dramatically fast necking instability via the elastic Considère mode in the nRP model for strain rates $\dot\epsilon>1/\tau_d$. Intuitively, as the sample starts to neck and the strain rate in the necking region increases,

the polymer is unable to provide any counterbalancing stress to restabilise the flow and the sample quickly fails.

In order for the elastic Considère mode of instability to arise in any given constitutive model, the 'loading' terms of that model, as represented by $\dot{\epsilon}f$ in the toy scalar version discussed above, must be sufficiently nonlinear that the 'elastic' force derivative $\partial_\epsilon F_{\text{elastic}}$, which is set by $-(\sigma_{\text{E}}^{+} - Gf)$, can become negative. For most models of polymeric flows that we have considered, in most flow regimes, this does not happen. In the nRP model, however, the loading dynamics has a (somewhat counterintuitive) negative contribution: in its toy representation, the loading term $f = 3 + 2Z - \frac{2}{3}Z^2$. The origin of the negative contribution lies in the assumption of instantaneous chain stretch relaxation $\tau_s \to 0$: what would be a chain stretch relaxation process with a finite associated timescale τ_s in the full sRP model is instead assumed to be infinitely fast in nRP, such that the chain stretch relaxes as quickly as it builds up with rate $\dot{\epsilon}$ in the flow. This leads to the apparent 'negative loading' term $-\frac{2}{3}\dot{\epsilon}Z^2$: it is actually a relaxation process, but occurring at the rate the sample is 'loaded' by strain. At high strain rates, this causes f to eventually become negative, sending $-(\sigma_{\text{E}}^{+} - Gf)$ and $\partial_\epsilon F_{\text{elastic}}$ negative, giving elastic Considère instability.

The stretching Rolie-Poly (sRP) model has a finite chain stretch relaxation timescale τ_s, which allows chain stretch to develop for strain rates $O(1/\tau_s)$ and above. Indeed, as noted above, in its raw form the sRP model displays an extensional catastrophe for strain rates $\dot{\epsilon} > 1/\tau_s$, with indefinitely increasing chain stretch and tensile stress. As in Oldroyd B, this indefinitely stabilises the filament against necking at imposed strain rates $\dot{\epsilon} > 1/\tau_s$: in Fig. 3e), no contour lines are crossed as the strain ϵ increases at these large strain rates (apart from mild transient growth, which quickly saturates). The introduction of "FENE" terms into the sRP model regularises this indefinite molecular stretching, rendering it finite and restoring necking instability at all strain rates (Fig. 3f).

The necking dynamics of the full Rolie-Poly model with finite chain stretch (Fig. 3f) therefore shows four distinct regimes, which can be summarised as follows. (I) For imposed strain rates $\dot{\epsilon} < 1/\tau_d$, gentle necking occurs right from the inception of the flow. (II) For strain rates in the regime $1/\tau_d < \dot{\epsilon} < 1/\tau_s$ the saturation of chain orientation associated with the flat region in the underlying constitutive curve places strong limitations on the tensile stress that the polymer can provide in any developing neck, giving more violent necking. This is a vestige in the fsRP model of the elastic Considère mode seen in the nRP model, although true elastic Considère doesn't arise with chain stretch. (III) For $\dot{\epsilon} = O(1/\tau_s)$ the rapid rise in chain stretch rate strongly mitigates necking, deferring it to a Hencky strain $\epsilon \approx 8$ for the parameter values considered here. Finally (IV) for $\dot{\epsilon} > 1/\tau_s$ the chain stretch saturates, leading to more rapid necking.

These four regimes of necking dynamics have strong signatures in the underlying homogeneous constitutive curve (Fig. 2f): the flatter this curve at any given strain rate, the more violent the necking at that imposed strain rate. Perhaps surprisingly, this is true even though the system in general does not have a chance to finally attain a state of steady homogeneous flow on the constitutive curve before it necks. This correspondence can, however, be motivated by a 'back of the envelope' calculation for a filament that does, in a thought experiment at least, manage to remain uniform long enough to attain a state of steady flow on its homogeneous constitutive curve, before starting to neck. A linear stability analysis for the dynamics of heterogeneous perturbations about this state of uniform steady flow then gives the linearised condition of mass balance

$$\dot{\delta a}_q = -\delta\dot{\epsilon}_q. \tag{VI.1}$$

The condition of force balance for a filament in a state of steady flow on its constitutive curve $\sigma_{\text{E}}(\dot{\epsilon})$ gives $\partial_u[a\sigma_{\text{E}}(\dot{\epsilon})] = 0$, which when linearised gives

$$0 = \sigma_{\text{E}}(\dot{\epsilon})\delta a_q + \sigma'_{\text{E}}(\dot{\epsilon})\delta\dot{\epsilon}_q, \tag{VI.2}$$

where prime denotes derivative with respect to the function's own argument. Combining these gives

$$\frac{\dot{\delta a}_q}{\delta a_q} = \frac{\sigma_{\text{E}}(\dot{\epsilon})}{\sigma'_{\text{E}}(\dot{\epsilon})}, \tag{VI.3}$$

with a growth rate given by $\sigma_{\text{E}}(\dot{\epsilon})/\sigma'_{\text{E}}(\dot{\epsilon})$. The necking at any given imposed strain rate is therefore faster the flatter the underlying constitutive curve at that strain rate, as seen in our numerical results. This can be understood physically as follows. Eqn. VI.1 states that in any region of a filament where the strain rate increases, the area decreases faster by mass conservation. Eqn. VI.2 states that in any such region where the area decreases, the strain rate must increase to provide an enhanced stress to maintain a uniform force along the filament. This gives a positive feedback loop and necking instability for any constitutive curve with a positive slope $\sigma'_{\text{E}}(\dot{\epsilon}) > 0$. The instability is furthermore faster the flatter the constitutive curve, because the strain rate must increase more quickly to provide an enhanced stress to maintain uniform force. Interestingly, a negative constitutive slope $\sigma'_{\text{E}}(\dot{\epsilon}) < 0$ is predicted to confer stability against necking, and we consider the implications of this more fully in [29].

The Pom-pom model of long chain branched polymers shows similar necking dynamics (Fig. 3g) to those just discussed for linear polymers. In particular we again see four distinct regimes, with (I): relatively gentle necking at low flow rates, (II): more rapid necking at moderate flow rates associated with the saturation in chain backbone orientation, (III): a degree of stabilisation against necking provided by developing backbone stretch, and finally (IV): more violent necking at higher strain rates due to a saturation in the degree of backbone stretch.

Two important differences between the Rolie-Poly model of linear polymers and the Pom-pom model of

branched polymers should however be noted. The first is that in the Pom-pom model the stress curvature criterion (shown by the thick black line in Fig. 3g), provides only a qualitative fit to the onset of necking (as characterised by a positive eigenvalue, shown by the thick dotted green line). This is because the expression for the polymer stress in the Pom-pom model contains multiplicative contributions from the chain orientation and chain stretch, each with its own dynamical evolution. (In contrast, the Rolie-Poly has just a single dynamical factor $W_{zz} - W_{xx} \equiv Z$ in the stress, as does the scalar model in which we derived the necking criteria.) As a result, the inflexion point $\ddot{\sigma}_{\rm E} = 0$ of the tensile stress provides only an approximation to the onset of necking in the Pom-pom model. Instead, it is the inflexion point in the component W_{zz} of molecular orientation that actually predicts onset. However this quantity cannot be accessed experimentally by measuring the tensile stress signal, because it appears in the expression for $\sigma_{\rm E}^{+}$ prefactored by the (also) time-evolving chain stretch.

The second difference is the appearance at high strain rates $\dot{\epsilon} > 1/\tau_s$ in the Pom-pom model of the elastic Considère mode, which was absent in the finite stretch Rolie-Poly model. This arises because the Pom-pom model invokes a hard cutoff for the growth in chain backbone stretch, to model its entropic limitation by the branching priority, q [69, 70]: the stretch is assumed to evolve only until it is equal to q and is held constant thereafter. This sharp saturation effectively removes the polymer's ability to provide any counterbalancing additional stress in any thinning region of the filament, leading to violent failure. This upper bound on the stretch imposed in the original form of the Pom-pom model [69, 70] is removed in some subsequent versions of the model (e.g. [75]), causing significantly different predictions for the necking dynamics. We comment further on the comparative necking dynamics predicted by these different assumed forms of backbone stretch dynamics in Sec. VII below.

We consider finally the necking dynamics of soft glassy materials (foams, emulsions, dense colloids, microgels, *etc.*) [31, 32]. These widely exhibit rheological ageing, in which (in the absence of an applied flow) a sample becomes progressively more solid-like and less liquid-like as a function of the time elapsed since it was prepared (for example by being freshly loaded into a rheometer and presheared). The fluidity model that we adopt captures ageing, predicting the stress relaxation timescale τ to increase linearly (in the absence of flow) as a function of the time since sample preparation. Here we consider a sample of age $t_{\rm w} = 1000\tau_0 = 1000$ (in our units) at the time the filament stretching run commences.

As seen in Fig. 3h), the sample necks by qualitatively different modes according to whether the imposed strain rate is fast or slow compared to the inverse sample age. In fast stretching $\dot{\epsilon} \gg 1/t_{\rm w}$, it fails violently via the elastic Considère mode. In slower stretching, $\dot{\epsilon} \ll 1/t_{\rm w}$, it fails more gradually, via a mode that is closely related to the stress curvature mode derived above in the scalar model: the stress curvature criterion is negative from the inception of flow for all $\dot{\epsilon}$. See [49] for further details. Put differently, for a fixed flow rate $\dot{\epsilon}$ a young sample $t_{\rm w} \ll 1/\dot{\epsilon}$ fails gradually, while an old sample $t_{\rm w} \gg 1/\dot{\epsilon}$ will fail more dramatically via the elastic Considère mode. This is the first instance, of which we are aware, in which a sample is predicted to fail by qualitatively different modes of necking instability according simply to its own age. The same picture also holds within the more sophisticated soft glassy rheology model [31, 32, 49].

In Fig. 3, then, we have shown our stress curvature and elastic Considère criteria to perform well in predicting the onset of necking in six widely used tensorial constitutive models of linear polymer solutions and melts, wormlike micelles, branched polymers, and soft glassy materials. They further perform well in distinguishing regions of relatively gradual necking, caused by the stress curvature mode, from the much more dramatic failure, caused by the elastic Considère mode.

Finally, in each panel of Fig. 3 we also mark as a blue long-dashed line the strain ϵ at which the tensile force overshoot occurs, in any filament stretching experiment at a fixed strain rate $\dot{\epsilon}$. For strains below this line, the force increases with strain. For strains above it, the force decreases and the original Considère predicts instability to necking. As can be seen, this original Considère criterion performs poorly in predicting the necking dynamics. For example, in Oldroyd B (which is however pathological in extension for the reasons discussed above) it fails to predict the strain rate $\dot{\epsilon} = 1/2\tau$ below which necking occurs and above which the filament is stable. (It instead incorrectly predicts this threshold to be $\dot{\epsilon} = 1/\tau$.) In the Giesekus, FENE-CR, finite-stretch Rolie-Poly and Pom-pom models it fails to predict the pronounced upward 'nose' shaped region of strains in which the sample is initially stable against necking, before necking sets in for larger strains. Finally in the non-stretch Rolie-Poly, Pom-pom and fluidity models the Considère criterion does nothing to distinguish between the slow, gradual necking that arises via the stress-curvature mode at low strain rates, and the much more dramatic failure due to the elastic Considère mode at higher strain rates. As noted above, however, the original Considère criterion converges towards our elastic Considère criterion (where present) in the limit of high strain rates $\dot{\epsilon}\tau \to \infty$, consistent with the fact that a complex fluid displays essentially solid-like response in this limit.

Effects of surface tension

So far, we have ignored the effects of surface tension. This is expected to be a good approximation in the initial stages of necking for most filament stretching experiments, because the samples used are typically highly viscoelastic and of sufficiently large radius that bulk stresses dominate surface ones. (Inevitably, surface tension must play some role during the final stages of pinchoff once the

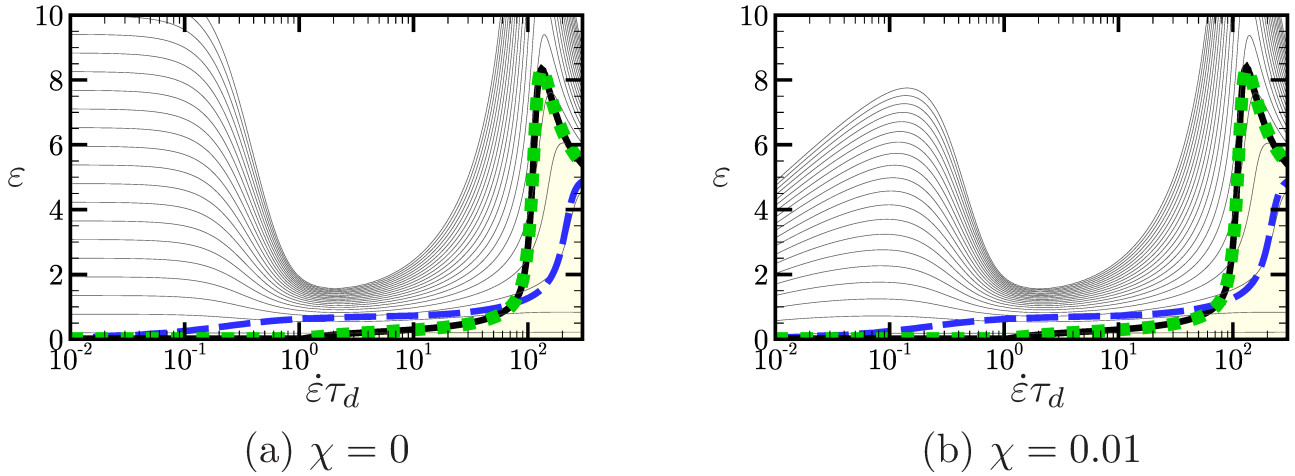

FIG. 4. Linearised necking dynamics in the Rolie-Poly model with finite chain stretch without surface tension (a) and with surface tension (b). Values of all other model parameters are the same as in Fig. 3f).

neck becomes very thin. However our slender filament calculations are not capable of capturing the details of pinchoff, and we do not consider this here.)

To quantify any effects of surface tension on the initial onset of necking, we recognise that its dominant effect is to give an additional contribution to the tensile stress of Eqn. III.9 [76], such that now

$$\sigma_{\rm E} = G\left(S_{zz} - S_{xx}\right) + 3\eta\dot{\varepsilon} + \frac{\chi}{r}. \qquad \text{(VI.4)}$$

Here χ is the coefficient of surface tension between the filament and surrounding fluid (usually air), and r is the time-evolving radius of the filament. (Here we use the leading order description of the mean curvature of the filament in the final term. The full expression [57] would introduce a $q-$dependence for the growth rate. However we do not expect this distinction to be important given our focus here on highly viscoelastic materials.)

In Fig. 4 we compare linear stability results for the Rolie-Poly model without surface tension (left panel) with those in a calculation where surface tension is now included. As can be seen, surface tension affects the onset of necking only at very slow flow rates. This is to be expected: in this regime the bulk viscoelastic stresses are relatively modest, and furthermore the sample survives to large strains before necking. This combination of a highly stretched sample of small radius and low bulk stresses means that the term χ/r is no longer small in comparison to the bulk viscoelastic stress $G\left(S_{zz} - S_{xx}\right)$.

We have checked that this effect of surface tension is essentially the same across all the models considered, affecting the onset of necking only in the regime of very slow flow rates. In view of this, we continue to neglect surface tension throughout the rest of the manuscript.

VII. NON-LINEAR SIMULATIONS

To examine the necking dynamics once the amplitude of heterogeneity has grown sufficiently that the linear calculations described in the previous section no longer provide a good approximation, the full nonlinear slender filament equations were numerically evolved. It is to the results of these nonlinear calculations that we now turn.

Recall that in the linear analysis we considered the dynamics of harmonic modes with wavelengths commensurate with the filament length. We thereby implicitly adopted periodic boundary conditions, effectively taking our filament to correspond to a torus being stretched. In reality, however, the filament has finite length and makes contact with a rheometer plate at each of its ends. The no-slip boundary condition that must be obeyed at the plates inevitably leads, during filament stretching, to a shear component in the flow field in the transition zone between the fluid that contacts the plates and the region of pure extensional stretching further from the plates.

This more complicated flow near each plate cannot be properly implemented at the level of our slender filament calculation, which only accounts for pure extensional flow. However a reasonable mimic of the no-slip condition can be achieved by employing the method suggested by Stokes et al. [77], whereby the background solvent viscosity is taken to diverge near the plates, thereby acting to 'pin' the fluid to the plates. The form of the divergence was derived, for a Newtonian fluid, by asymptotically matching a lubrication solution near each plate with a slender filament approximation far from the plates, and is as follows:

$$\eta(u) = \eta\left[1 + \frac{1}{32}\left(\frac{r_0 e^{-\bar{\epsilon}}}{u}\right)^2 + \frac{1}{32}\left(\frac{r_0 e^{-\bar{\epsilon}}}{1-u}\right)^2\right], \qquad \text{(VII.1)}$$

where r_0 is the initial radius of the sample. (In principle this form should be rederived for each given constitutive

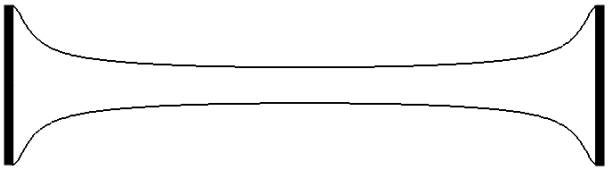

FIG. 5. Effect of the no-slip boundary condition at the rheometer plates in seeding heterogeneity even before any true material instability causes significant necking. Outline shows a purely Newtonian fluid stretched to a Hencky strain $\epsilon = 2.0$, within our 1D slender filament approach.

equation in turn, but that task would be prohibitively complicated and we do not tackle it here. We assume instead that this form provides a reasonable model of the essential physics for non-Newtonian fluids too.) Imposing this boundary condition sets the strain rate at each end-plate to zero. In this way the filament area remains pinned to its initial value at each plate, and no viscoelastic stress develops there. The fluid velocity exactly follows that of the plates.

Even in the absence of a true necking instability, this boundary condition will lead to the development of some spatial heterogeneity during filament stretching: the region of fluid near each plate is essentially prevented from stretching properly, so the central region of the filament thins proportionately more quickly (Fig 5).

In view of this, one might in fact question the basis of our linear stability calculations in Secs. IV to VI, which assumed the filament to stretch in a purely uniform way before any true necking instability arises. However the heterogeneity arising from the no-slip condition tends to be localised near the plates, with the central region remaining relatively uniform until necking arises. The criteria of Sec. V should therefore still be expected to hold, provided they are calculated using the material functions in the central region of the filament, well away from the plates. Nonetheless, it is reasonable to assume that the dominant source of any initial heterogeneity that later becomes exponentially amplified by the necking instability will be this endplate effect.

With these boundary conditions, we numerically evolve the nonlinear slender filament equations III.14 to III.17. The fact that these are already expressed in the coextending frame removes any need for remeshing the numerical grid as the filament stretches. Therefore we discretize the equations on a fixed mesh of grid points and time-step the equations using an explicit Euler algorithm for the spatially local terms and 1st order upwinding for the convective terms [78], with results checked against a 3rd order upwinding scheme. Care is taken to ensure convergence of the results with respect to increasing the number of grid points N and decreasing the timestep Δt. Generally $N = 1500$ is sufficient, although in some cases $N = 2000$ is required. A timestep $\Delta = 1/2N^2$ is usually adequate, but in the case of violent necking we employ an adaptive time stepping algorithm in which the values of the stress and area after a single time-step Δt are compared to the corresponding values after two half timesteps $\Delta t/2$. If the difference between these values exceeds a certain tolerance, Δt is halved and the procedure repeated until the tolerance met.

With these remarks in mind, we now present our results. The nonlinear necking dynamics of soft glassy materials were reported previously in Ref. [49], so we focus here on polymeric fluids. We consider both entangled linear polymers (and wormlike micelles), studied using the Rolie-Poly model; and entangled branched polymers, studied using the Pom-pom model.

A. Entangled linear polymers

In this section we consider entangled linear polymeric fluids (polymers and wormlike micelles) described by the Rolie-Poly model with finite chain stretch. We study a highly entangled sample with entanglement number $Z = 40$, which gives a chain stretch relaxation time $\tau_s = \tau_d/3Z = 0.00833$ in our units. The values of the other model parameters are detailed in App. A 4.

The results of our nonlinear slender filament simulations are shown in Fig. 6. Panel a) shows the equivalent, for these nonlinear calculations, of the linear stability data discussed previously in Fig. 3f). As before, a vertical cut up this plane of strain ϵ and strain rate $\dot{\epsilon}$ represents a single filament stretching run performed at a given imposed strain rate $\dot{\epsilon}$, starting with an unstretched filament at $\epsilon = 0$, and with the filament being progressively stretched out as the accumulated strain ϵ increases upward. Recall the accumulated strain ϵ is trivially related to the time t since the inception of the flow by the relation $\epsilon = \dot{\epsilon}t$, in this constant strain rate protocol. In what follows, we sometimes find it convenient to refer to time and sometimes strain.

The thin black lines in Fig. 6a) show contours of constant $\Lambda(t) \equiv A_{\rm hom}(t)/A_{\rm mid}(t)$, where $A_{\rm hom}(t)$ is the filament area calculated at any time t by supposing the filament were stretching in a purely uniform way, and $A_{\rm mid}(t)$ is the actual cross sectional area at the filament's midpoint. In this way, $\Lambda = 1$ corresponds to a uniform filament, and Λ progressively increases as the filament necks. In the figure the first contour has $\Lambda = 1$, and each successive contour crossing as ϵ increases upwards at fixed $\dot{\epsilon}$ corresponds to an increase in Λ by a factor $4^{1/20}$, such that the $20th$ contour, which is the final shown, represents $\Lambda = 4$. (Although this ratio of areas is relatively modest we note that the sample is close to necking by this time, because the global area has become very small.) The more densely clustered the contour lines vertically at any fixed $\dot{\epsilon}$, therefore, the faster necking occurs in a filament stretching experiment at that strain rate. We have shown only the first 20 contour lines, assuming that the sample will have failed altogether by the time this contour is attained. (We recall, however, that our slender filament calculation is not capable of capturing the

details of final pinchoff.)

Also included in Fig. 6a), as in Fig. 3f), is a green dotted line showing the strain ϵ at which the largest eigenvalue (calculated using the values of the material functions at the filament's midpoint) first becomes positive in any filament stretching experiment at a given strain rate $\dot{\epsilon}$, signifying the onset of instability to necking. The thick black solid line depicts the strain at which the stress curvature criterion (V.18) predicts this onset. For strains below this black line, the true tensile stress (calculated at the filament's midpoint) is an upwardly curving function of time (or accumulated imposed strain). For strains above it, the stress curves downward in time. As can be seen, our stress curvature criterion performs well in predicting the onset of necking (rapid crossing of Λ contours). Some contour crossing (growth in Λ) does however occur before true onset, mainly because of the endplate effects discussed above.

Comparing Fig. 6a) with Fig. 3f), we see that our simplified linear calculation (which assumed a perfectly uniform base state prior to the onset of necking, together with simplified periodic boundary conditions), already performed rather well in predicting the onset of necking in the full nonlinear calculations. All the features of Fig. 3f) are preserved in Fig. 6a), with any small quantitative differences being explained by the fact that the material functions at the filament's midpoint in the nonlinear simulations differ slightly from those in an initially perfectly uniform filament.

The blue long-dashed line in Fig. 6a) shows the strain ϵ at which the tensile force overshoot occurs. For strains below this line, the force increases with strain. For strains above it, the force decreases and the original Considère criterion predicts instability to necking. As can be seen, the Considère criterion performs poorly compared to our stress curvature criterion. For example, it fails to predict the pronounced nose-shaped window of prolonged stability at imposed strain rates $\epsilon = O(1/\tau_R)$. It also contains no information about the rate of growth beyond onset, which our calculation provides.

The necking dynamics at the six imposed strain rate values denoted by over-arrows in Fig. 6a) are studied in detail in panels b) and c). At each strain rate, the symbols in panel b) show the time-evolution of the apparent extensional stress growth coefficient $\eta^+_{\mathrm{E,app}}(t) = F(t)/\dot{\epsilon}A_{\mathrm{hom}}(t)$. Recall that this is defined as the tensile force $F(t)$ normalised by the constant imposed strain rate $\dot{\epsilon}$ and the time-evolving cross sectional area $A_{\mathrm{hom}}(t) = A(0)L(0)/L(t) = A(0)\exp(-\epsilon)$ as calculated supposing uniform stretching, without necking or endplate effects. It is this measure of extensional stress that would be reported in a filament stretching experiment that did not explicitly measure changes in the filament's cross sectional area due to necking. For comparison we also show by solid lines in panel b) the stress growth coefficient calculated by assuming (incorrectly) that the filament remains uniform during stretching. As can be seen, when necking sets in the measured apparent stress growth coefficient decreases compared to that of the purely homogeneous calculation, because of a reduction in the force $F(t)$ as the filament thins in the neck. Such curves show a close resemblance to experimental ones, for example in [22]. For the same six values of imposed strain rate, panel Fig. 6c) shows the time-evolution of the cross sectional area at the filament's midpoint as a function of accumulated strain. Also shown by a solid line for comparison is the area evolution $A(t) = A(0)\exp(-\epsilon)$ supposing perfectly uniform stretching.

Recalling our discussion in Sec. VI above about the four different regimes of necking dynamics predicted by the Rolie-Poly model, the results of Fig. 6 can be summarised as follows.

For small imposed strain rates $\dot{\epsilon} < 1/\tau_d = 1$ (in our units) the stress curvature criterion is satisfied, and filament is unstable to necking, straight away from the inception of the flow. However the rate of development of the neck is rather modest, $O(\dot{\epsilon})$, giving relatively widely spaced contours of constant Λ in Fig. 6a): the cross sectional area $A_{\mathrm{mid}}(t)$ at the filament midpoint (red dashed line in Fig. 6c) deviates relatively gradually from the area $A_{\mathrm{hom}}(t) = A(0)L(0)/L(t)$ that would be expected assuming purely uniform stretching (black solid line), and a strain $\epsilon \approx 6$ is attained before significant necking occurs. In contrast, the tensile stress attains a steady state on the homogeneous constitutive curve after a strain of only $\epsilon \approx 1$ at these slow imposed strain rates. A meaningful measurement of the constitutive curve can therefore be taken before necking occurs: the red symbols in Fig. 6b) display a window of steady state between $t = 10$ and 30 before the stress then falls due to necking.

For imposed strain rates in the regime $1/\tau_d < \dot{\epsilon} < 1/\tau_R$ the stress curvature criterion is again satisfied, and the filament is unstable to necking, right from the inception of the flow. However in this regime the neck develops much more rapidly, as seen by the closely spaced contours in panel a), consistent with the sudden fall at a strain $\epsilon \approx 1.5$ in Fig. 6b) of the actual cross sectional area at the filament's midpoint (green line) from the area evolution calculated supposing uniform stretching (black line). As discussed in Sec. 3, this violent necking behaviour is consistent with the flat region in the material's underlying constitutive curve in this regime of strain rates (Fig. 2f), associated with the saturation of chain orientation for $\dot{\epsilon} > 1/\tau_d$ and the absence of any significant chain stretch for $\dot{\epsilon} < 1/\tau_R$. These two factors combine to place strong limitations on any tensile stress that the polymer can provide to restabilise any developing neck. As a result of this rapid necking, the tensile stress does not have time to attain a steady state on the homogeneous constitutive curve before significant heterogeneity develops: the green symbols depart from the green line in Fig. 6b) before steady state is attained.

At larger strain rates $O(1/\tau_R)$, significant chain stretch can develop and provide additional tensile stress, consistent with the steep slope of the underlying constitutive curve in this window of strain rates in Fig. 2f). This ad-

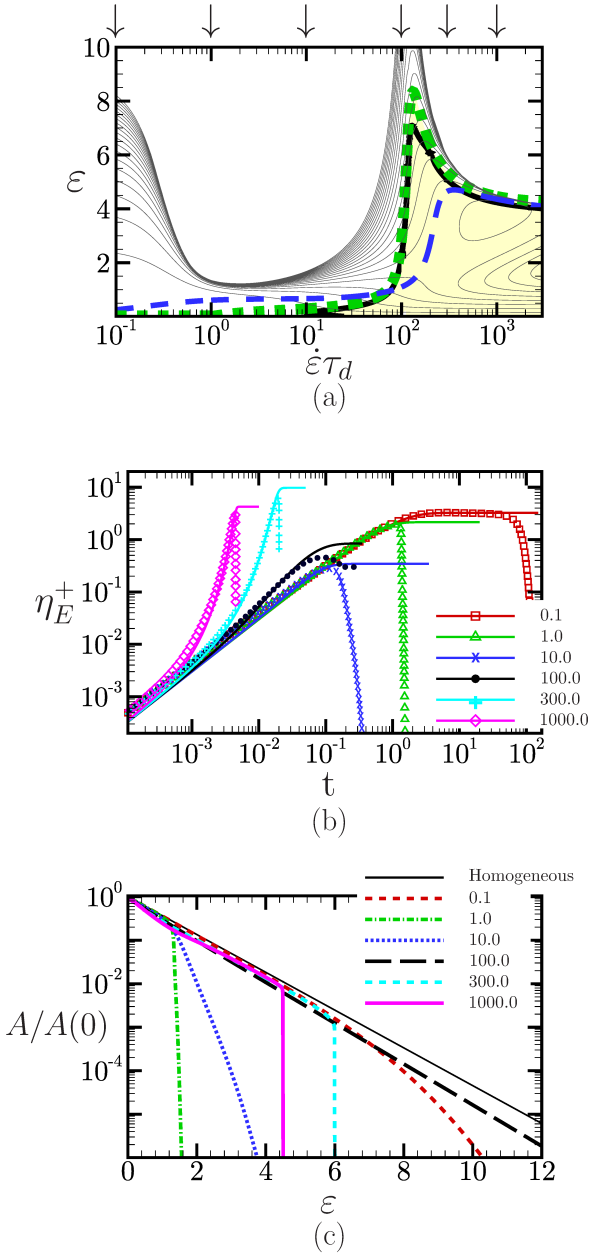

FIG. 6. Necking dynamics in nonlinear slender filament simulations of the Rolie-Poly model of linear entangled polymeric fluids. (a) Thin black lines show contours of the degree of necking heterogeneity. Also shown are the criteria of Sec. IV, calculated using values of rheological functions at the filament's midpoint: onset of positive eigenvalue to necking (green dotted line), stress curvature criterion (thick black line) and original Considère criterion (blue long dashed line). For the six imposed strain rates indicated by arrows in (a), the apparent stress growth coefficient is reported in (b) for both the nonlinear simulation (symbols) and for a calculation in which the filament is artificially assumed to remain uniform. Counterpart results for the filament's cross sectional area are shown in (c): assuming homogeneous flow (solid black line) and allowing for necking (broken lines).

ditional stress provides some stabilisation against necking and the onset of necking is deferred until a finite strain has accumulated after the inception of the flow, as seen by the 'upward nose' in the green and black lines in Fig. 6a). This is consistent with the data in Fig. 6c) for an imposed strain rate $\dot{\epsilon} = 100.0$, which shows the area at the filament's midpoint remaining rather close to that calculated assuming uniform deformation even up to a strain $\epsilon = 8.0$. (Indeed, some stabilisation effect due to chain stretch can already be seen at a strain rate $\dot{\epsilon} = 10.0$, by comparing the blue and green curves in Fig. 6c.) However, in this regime of strain rates a typical strain $\epsilon \approx 10.0$ would be required for the tensile stress to attain the homogeneous constitutive curve (in a thought experiment

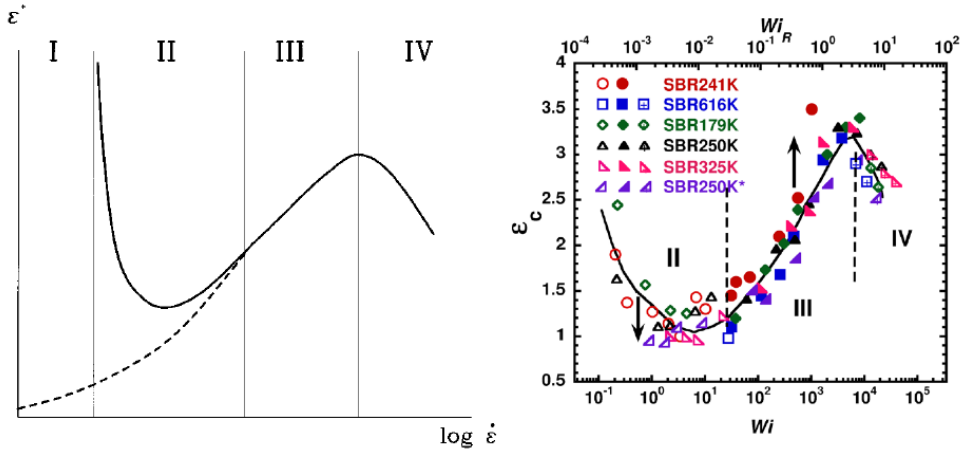

FIG. 7. Left) Sketch of strain to failure in filament stretching as a function of imposed strain rate, from [43]. Right) Master curve of experimental data showing strain to failure in filament stretching as a function of imposed strain rate, from [79]. (Strain rate shown in units of inverse reptation time, as in our calculations.

where the filament remained uniform), as seen by the black solid line in panel b). Because of this, a meaningful measurement of the constitutive curve still cannot be taken before the filament necks and the stress declines (black symbols in panel b) compared to that in the homogeneous calculation. Note that the overshoot shown by the black symbols in panel b) is in the *apparent* stress growth coefficient, and stems from the decline in tensile force as the filament fails at the neck. The Rolie-Poly model lacks any overshoot in the *true* stress growth coefficient (Fig. 1).

Finally for $\dot{\epsilon} > 1/\tau_s$ the chain stretch saturates and the additional tensile stress that can be provided by this mechanism levels off, as seen in the constitutive curve in Fig. 2f) at high strain rates. Therefore the polymer is once again unable to supply additional stress to restabilise any developing neck, leading to more sudden filament failure (cyan and magenta symbols in panel b) and lines in panel c).

In the experimental literature, the strain at which a sample fails is often discussed in terms of a master curve, plotted as a function of imposed strain rate. This was introduced as a sketch [19, 43], which we reproduce here in Fig. 7(left). Experimental data [79, 80] were collected into such a curve for a styrene-butadiene random (SBR) copolymer linear melt in [79], reproduced here in Fig. 7(right). The four different regimes in this master plot were suggested by by [19, 43] to be interpreted as I "flow"; II "transition"; III "rubbery" and IV "glassy". Based on our results in Figs. 2f), 3f) and 6, however, we now suggest that these four regimes can in fact be fully interpreted within the Rolie-Poly model as I: a slow flow regime with gentle necking for $\dot{\epsilon} < 1/\tau_d$; II: a regime in which the chain orientation saturates, leading to fast necking for $1/\tau_d < \dot{\epsilon} < 1/\tau_R$; III: a regime of increasing molecular stretch, which provides some stabilisation against necking for $\dot{\epsilon} = O(1/\tau_R)$; and IV: a regime in which the molecular stretch saturates, leading again to more rapid necking for $\dot{\epsilon} > 1/\tau_R$. In particular the form of a representative contour in Fig. 6a), characterising the typical strain to failure, is in overall agreement with the experimental curves in both subfigure shown in Fig. 7.

B. Branched polymers

We now turn to the necking dynamics of branched polymers as modelled by the Pom-pom constitutive equation of App. A 5. We perform calculations separately for the two sets of model parameters listed in that appendix: PP1, describing a highly branched sample with a number of arms $q = 40$ attached to each end of the molecular backbone; and PP2, with $q = 5$.

We consider first PP1, for which the underlying homogeneous extensional constitutive curve was shown in Fig. 2g), and the predictions of our linear stability calculations were shown in 3g). The counterpart results of our full nonlinear slender filament simulations are shown in Fig. 8(a,c,e), in the corresponding format to the results of Fig. 6 for the Rolie-Poly model.

As can be seen, the linear stability calculation of Fig. 3g) again performs rather well in predicting the full nonlinear necking dynamics of the Pom-pom model, despite having considered the simpler case of small perturbations about a perfectly uniform filament with periodic boundary conditions. As is evident, the stress curvature criterion determines the onset of necking for low and moderate strain rates, before the elastic Considère criterion takes over at high strain rates. Furthermore, the four regimes of strain rate discussed above in the context of linear polymers are mirrored here for the branched polymers, as follows.

For imposed strain rates $\dot{\epsilon} < 1/\tau_b$, where τ_b is the timescale for reorientation of the chain backbone, we see

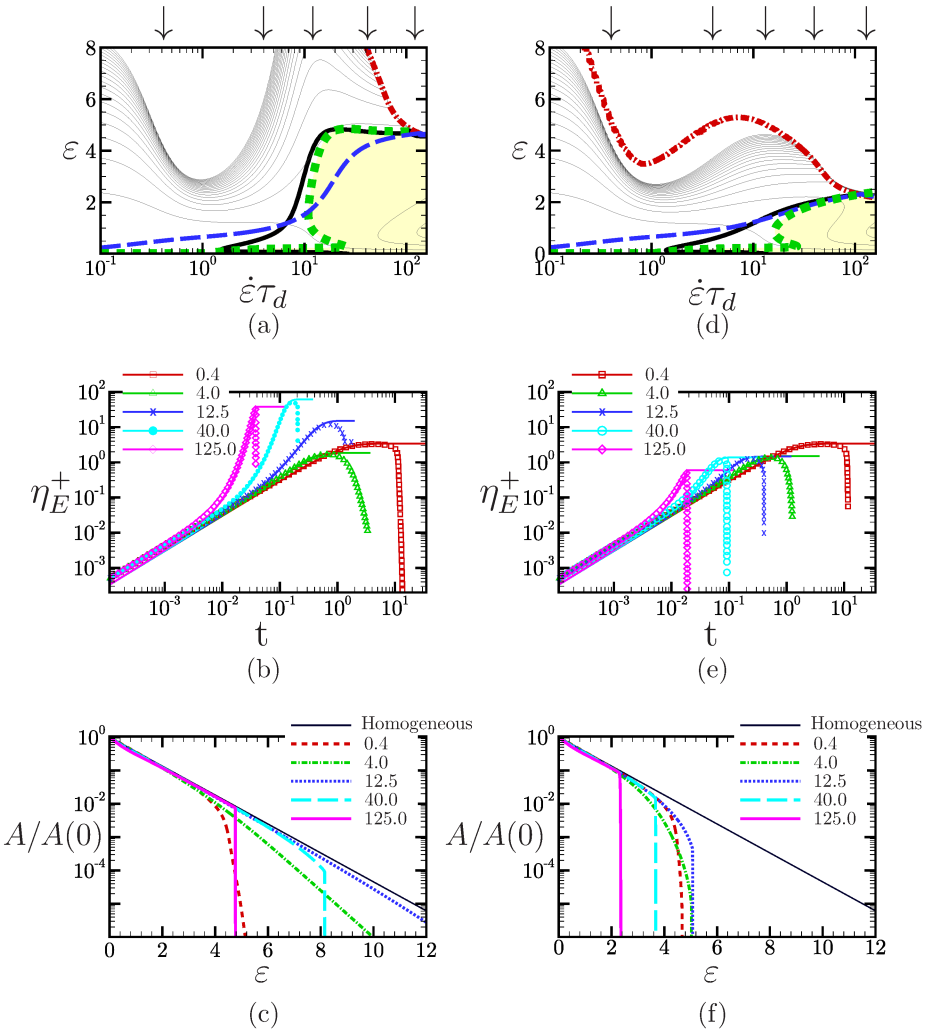

FIG. 8. Counterpart of Fig. 6, now for the Pom-pom model of branched polymers. Sub-figure (a)-(c) pertain to sample PP1 and sub-figures (d)-(f) to sample PP2. Model parameter values for each sample are given in App. A.

a regime of relatively gentle necking instability that is effective right from the inception of flow, triggered by the stress curvature criterion: the stress signal curves downward as a function of time for all times $t > 0$, as seen by the thick black line at $\epsilon = 0$ for these strain rates.

For the window of imposed strain rates $1/\tau_b < \dot{\epsilon} < 1/\tau_s$, where τ_s is the timescale for relaxation of backbone stretch, we find more rapid necking. This is due to the fact that backbone reorientation has saturated in this regime and is therefore unable to provide a counterbalancing tensile stress in any developing neck. This is consistent with the flat region in the underlying constitutive curve of Fig. 2g) in this window of strain rates $1/\tau_b < \dot{\epsilon} < 1/\tau_s$. This window is however smaller for PP1 in Fig. 8a) than in the Rolie-Poly calculations of Fig. 6, because we assume that the higher drag afforded by the dangling arms slows down the relaxation of the backbone stretch relative to reorientation. The strain at which significant necking occurs for the most unstable strain rate is accordingly around 3.0 in PP1, compared to around 1.5 for the Rolie-Poly model.

For imposed strain rates $\dot{\epsilon} = O(1/\tau_s)$ significant backbone stretch develops, consistent with the strong slope in the underlying constitutive curve of Fig. 2g) for such strain rates. As in linear polymers, this can provide an additional tensile stress and act temporarily to stabilise the filament against necking over a finite window of accumulated strain after the inception of flow. This is evident in the upswing in the black solid and green dashed lines at $\dot{\epsilon}\tau_b \approx 10.0$ in Fig. 8a). At small times (or accumulated strains) the stress curves upward as a function of time (or strain), consistent with the filament being stable against necking. Only after a finite strain has accumulated does the stress curve downward and trigger instability.

For the highest strain rates $\dot{\epsilon} > \tau_s$ the chain stretch saturates, the underlying constitutive curve flattens out, and the stabilisation mechanism just described is lost. Indeed, in the original version of the Pom-pom model a hard cutoff is imposed in the degree of backbone stretch that can develop, with the stretch taken to be entrop-

ically limited by the branching priority, $\lambda \leq q$. This pronounced nonlinearity results in the elastic Considère mode of necking instability setting in at these high strain rates, at a strain denoted by the red dot-dashed line in Fig. 8). Once active, this mode leads to to catastrophically fast necking.

Consistent with this discussion of the different necking regimes, in the time-signals of the apparent stress growth coefficient and the cross sectional area at the filament's midpoint (Figs. 8b,c) we again see relatively smooth necking at low strain rates, with much more violent failure at high strain rate.

As in the Rolie-Poly model, the original Considère criterion (blue long dashed line in Fig. 8a) performs less well compared to our calculations in determining the onset of necking. For example, it cannot predict the pronounced upswing of stability against necking around $\dot{\epsilon} = 10.0$ evidenced by our stress curvature criterion (black solid line) and eigenvalue calculations (green dashed line). It says nothing of the rate at which a neck develops once instability sets in, and thereby fails (for example) to distinguish between the relatively gentle necking for imposed flow rates $\dot{\epsilon} < 1/\tau_b$ compared to the faster necking for $1/\tau_b < \dot{\epsilon} < 1/\tau_s$. Finally, it fails to distinguish between the two different modes of instability that we predict: stress curvature at low strain to moderate strain rates, and elastic Considère at high strain rates. At high strain rates, however, the onset of the original Considère mode does coincide with that of our elastic Considère mode, consistent with the material behaving essentially like an elastic solid in this regime.

A close comparison of Figs. 3g) and 8a) reveals a greater effect of the elastic Considère mode in the nonlinear simulations than in the linear ones, with the red dashed line extending to lower imposed strain rates in Fig. 8a). The reason for this is as follows. In the linear calculation, the background strain rate used to calculate the instability criteria is fixed throughout the whole run, with any necking perturbations that arise being infinitesimal in comparison (by definition of the linearisation). In contrast, the nonlinear calculation does account for changes to the rheological quantities in the developing neck. In particular, because the neck (by definition) thins faster than the surrounding material, the fluid within it becomes subject to a larger strain rate than the globally imposed one. After some time of necking via the stress curvature mode, therefore, it suffers elastic Considère at a lower globally imposed strain rate than would be predicted by the linear calculation alone.

Results for sample PP2 with fewer arms, $q = 5$, are shown in Fig. 8(d)-(f). The same four regimes as for PP1 and the Rolie-Poly model are again evident, though with slightly less well separated features. The shift in the elastic Considère threshold compared to that in the linear calculations is particularly pronounced in this case, due to the much stronger effect of the hard cutoff in λ for this smaller q. In consequence, after an interval of necking via the stress curvature mode, the region of material in the neck would eventually succumb to the elastic Considère mode at any value of the globally imposed strain rate. For strain rate less then around 20.0, however, this may be unimportant because the sample will in practice have failed altogether via the stress curvature mode before the elastic Considère mode has chance to set in.

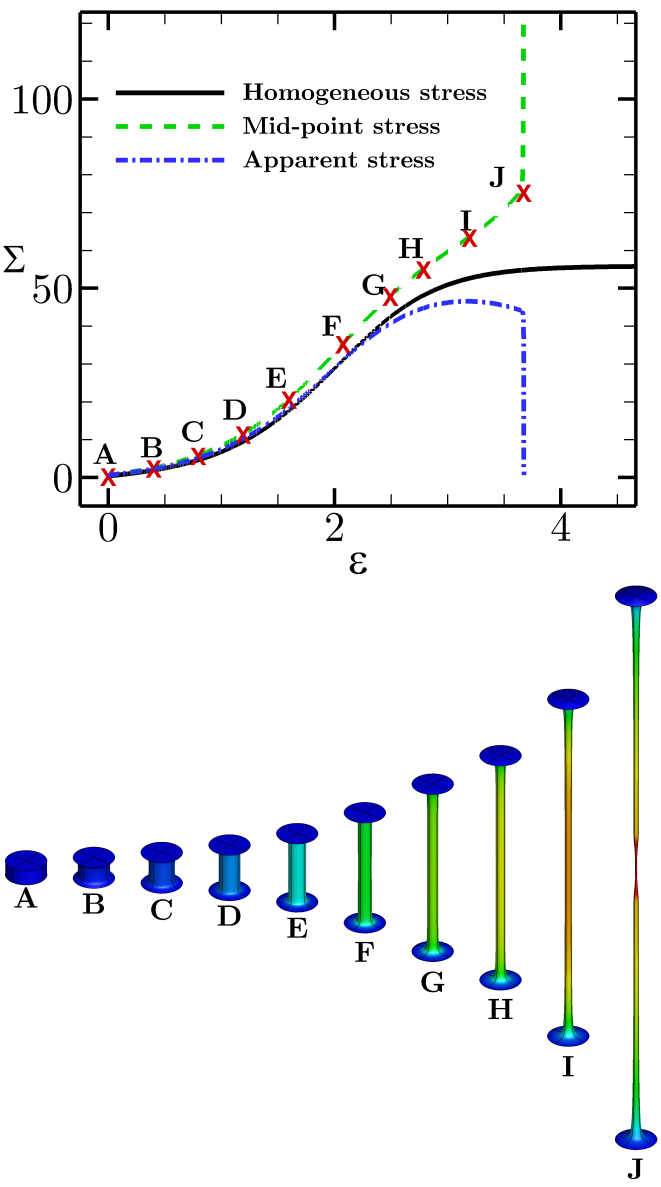

FIG. 9. (a) Apparent (dash-dot line) and true mid-point (dotted line) extensional stress growth coefficients versus time in the Pom-pom model (PP2) at a imposed strain rate $\dot{\epsilon} = 40.0$. Solid line shows the same quantity in a calculation that artificially constrains the filament to remain uniform. (b) Profile snapshots at the times indicated in (a), with the colourscale showing the tensile stress.

The detailed necking dynamics for $q = 5$ at an imposed strain rate $\dot{\epsilon} = 40.0$ are shown in Fig. 9. Panel a) shows as dashed, dash-dot and solid lines respectively the

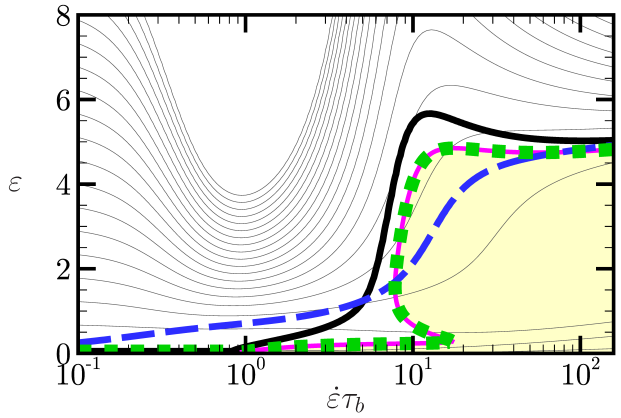

FIG. 10. Counterpart to Fig. 8a) for the Pom-pom model with parameter values PP1, but with the cutoff condition on chain stretch removed.

mid-point true stress, apparent stress and (artificial) homogeneous stress growth coefficient as a function of accumulated strain $\epsilon = \dot{\epsilon}t$ in our necking simulation. (Recall the definition of these coefficients at the end of Sec. I.) Panel b) shows snapshots of the filament's profile, with the tensile stress represented by the colour scale. (Although the profiles are graphically rendered in 3D, recall that our calculations are performed in 1D.) As can be seen, at early times (profiles a-f), the filament area and tensile stress are uniform along filament, apart from in a small region due to the (mimicked) no-slip condition near each endplate. Once the stress curvature mode sets in at a strain $\epsilon \approx 2.0$ the stress profile starts to become inhomogeneous. Finally, the elastic Considère criterion is satisfied at the filament's midpoint around a strain $\epsilon \approx 3.2$ and the sample quickly fails.

It is worth noting, however, that the presence of a true elastic Considère mode in the Pom-pom model relies on the hard cutoff in backbone stretch imposed in the original version of the model as proposed by [69, 70]. Versions of the model proposed since, for example in Ref. [75], remove this upper bound in the backbone stretch. Therefore for comparison with our results shown in Fig. 8 for the hard cutoff, we show in Fig. 10 counterpart (linear stability) results (for PP1) with the maximum stretch limit removed as in [75]. As can be seen, this removes the elastic Considère mode and gives very much gentler necking even at high imposed strain rates. However experimental evidence (e.g. [22]) suggests that branched materials do show a rather sudden rupture at sufficiently high strain rates. This may indicate a harder saturation in backbone stretch than is accounted for in [75]. Indeed, we suggest that the severity of necking may help to shed some light on the appropriate form of model dynamics in this regime.

VIII. CONCLUSIONS

We have studied the necking dynamics of a filament of viscoelastic material subject to uniaxial tensile stretching. By means of a linear stability analysis performed in a constitutive equation written in highly general form, we have predicted criteria for the onset of necking that can be expressed simply in terms of characteristic signatures in the shapes of the experimentally measured rheological response functions. Given the highly generalised nature of this calculation, we suggest that the criteria offered here might be expected to apply universally to all materials. We have provided evidence for their generality by showing them to apply in numerical calculations of six popularly used constitutive models: Oldroyd B, Giesekus, FENE-CR, Rolie-Poly, Pom-pom and a fluidity model of soft glassy materials.

Two distinct modes of necking instability are predicted. The first sets in when the tensile stress signal first curves downward as a function of the time (or accumulated strain) since the inception of the flow. Once active, it causes necking with a relatively gentle rate of development. The second mode sets in when a carefully defined 'elastic derivative' of the tensile force first slopes downward as a function of time (or strain), and gives much more violent failure. Whether this 'elastic derivative' has any easily measurable experimental counterpart remains an open question. Nonetheless, in the limit of large strain rate $\dot{\epsilon}\tau \to \infty$ the elastic derivative tends towards the ordinary time (or strain) derivative of the tensile force, and our elastic Considère criterion reduces to the widely discussed Considère criterion for necking in solids. An important contribution of this work, however, is to show that the original Considère criterion fails to correctly predict the onset of necking in the regime of viscoelastic flows at finite imposed flow rates $\dot{\epsilon}\tau$. Those parts of the rheology literature that have discussed necking onset in terms of the Considère criterion might therefore warrant some reinterpretation.

We have studied in detail the way in which our two modes of necking instability manifest themselves within the microscopically motivated Rolie-Poly model of entangled linear polymers and wormlike micelles, and the Pom-pom model of entangled branched polymers. In particular, we have demonstrated four distinct regimes of necking dynamics, depending on the value of the imposed strain rate relative to the inverse reptation and stretch relaxation times. Our theoretically predicted curve of strain-to-failure as a function of imposed strain rate is consistent with master curves reported in the experimental literature [19, 43, 79, 80].

Throughout we have made the simplifying assumption that spatial variations develop only along the length of the filament z, within a one-dimensional (1D) slender filament approach that averages (at any z) across the filament's radius r and assumes no variations in the angular coordinate θ. A comparison of 1D (z) and 2D (rz) simulations of viscoelastic extensional flows of di-

lute and semi-dilute polymer solutions was carried out in [52] where, surprisingly, the 1D approach was found to compare better with experiment. Simulation studies of θ dependent effects near the endplates were performed in Ref. [81, 82]. These are beyond the scope of this work, and we hope would not affect the necking dynamics well away from the endplates, which has been our focus here.

This manuscript has concerned necking at constant imposed Hencky strain rate. In a separate manuscript [29] we consider the protocols of constant imposed tensile stress, and constant imposed tensile force.

We hope that our calculations will stimulate experimental work to confirm (or disprove) the criteria offered here, potentially enabling the rheology community to move beyond the interpretation of necking in complex fluids in terms of the Considère criterion for necking in solids. It would be particularly interesting to determine whether the appearance of an inflexion point (and subsequent downward curvature) in the tensile stress signal indeed acts as a trigger for the onset of necking.

Acknowledgements – The research leading to these results has received funding from the European Research Council under the European Union's Seventh Framework Programme (FP7/2007-2013) / ERC grant agreement number 279365. The authors thank Gareth McKinley for suggesting that they work on this problem; and Ole Hassager, Joe Leeman, and Tom McLeish for interesting discussions.

---

* d.m.hoyle@durham.ac.uk; http://community.dur.ac.uk/d.m.hoyle/
† suzanne.fielding@durham.ac.uk; http://community.dur.ac.uk/suzanne.fielding/

[1] D. M Hoyle, Q Huang, D. W Auhl, D. G Hassell, H. K Rasmussen, A. L Skov, O. G Harlen, O Hassager, and T. C. B McLeish. Transient overshoot extensional rheology of long chain branched polyethylenes: experimental and numerical comparisons between filament stretching and cross-slot flow. *Journal of Rheology*, 57(1):293–313, 2013.

[2] S. J Haward, M. S. N Oliveira, M. A Alves, and G. H McKinley. Optimized Cross-Slot Flow Geometry for Microfluidic Extensional Rheometry. *Physical Review Letters*, 109(12):128301, sep 2012.

[3] F. J Galindo-Rosales, M. A Alves, and M. S. N Oliveira. Microdevices for extensional rheometry of low viscosity elastic liquids: a review. *Microfluidics and Nanofluidics*, 14(1-2):1–19, jan 2013.

[4] G. H McKinley and T Sridhar. Filament-Stretching Rheometry of Complex Fluids. *Annual Review of Fluid Mechanics*, 34(1):375–415, 2002.

[5] H Münstedt. Viscoelasticity of polystyrene melts in tensile creep experiments. *Rheologica Acta*, 14:1077–1088, 1975.

[6] H Münstedt and Z Starý. Steady states in extensional flow of strain hardening polymer melts and the uncertainties of their determination. *Journal of Rheology*, 57 (4):1065, 2013.

[7] H Münstedt. Rheological experiments at constant stress as efficient method to characterize polymeric materials. *Journal of Rheology*, 58(3):565–587, 2014.

[8] N. J Alvarez, J Marín, Q Huang, M Michelsen, and O Hassager. Creep Measurements Confirm Steady Flow after Stress Maximum in Extension of Branched Polymer Melts. *Physical Review Letters*, 110(16):168301, apr 2013.

[9] M. H Wagner, H Bastian, A Bernnat, S Kurzbeck, and C. K Chai. Determination of elongational viscosity of polymer melts by RME and Rheotens experiments. *Rheologica Acta*, 41(4):316–325, may 2002.

[10] P Szabo, G. H McKinley, and C Clasen. Constant force extensional rheometry of polymer solutions. *Journal of Non-Newtonian Fluid Mechanics*, 169-170:26–41, feb 2012.

[11] V. C Barroso and J. M Maia. Influence of long-chain branching on the rheological behavior of polyethylene in shear and extensional flow. *Polymer Engineering & Science*, 45(7):984–997, jul 2005.

[12] G Liu, H Ma, H Lee, H Xu, S Cheng, H Sun, T Chang, R. P Quirk, and S.-Q Wang. Long-chain branched polymers to prolong homogeneous stretching and to resist melt breakup. *Polymer*, 54(24):6608–6616, 2013.

[13] T. I Burghelea, Z Starý, and H Münstedt. On the viscosity overshoot during the uniaxial extension of a low density polyethylene. *Journal of Non-Newtonian Fluid Mechanics*, 166(19-20):1198–1209, oct 2011.

[14] A Tripathi, K. C Tam, and G. H McKinley. Rheology and Dynamics of Associate Polymer Solutions in Shear and Extension: Theory and Experiments. *Macromolecules*, 39:1981–1999, 2006.

[15] A Bhardwaj, E Miller, and J. P Rothstein. Filament stretching and capillary breakup extensional rheometry measurements of viscoelastic wormlike micelle solutions. *Journal of Rheology*, 51(2007):693, 2007.

[16] M Arciniaga, C.-C Kuo, and M Dennin. Size dependent brittle to ductile transition in bubble rafts. *Colloids and Surfaces A: Physicochemical and engineering aspects*, 382 (1-3):36–41, jun 2011.

[17] M. I Smith, R Besseling, M. E Cates, and V Bertola. Dilatancy in the flow and fracture of stretched colloidal suspensions. *Nature communications*, 1(8):114, jan 2010.

[18] R. J Andrade and J. M Maia. A study on the flow, failure, and rupture mechanisms of low-density polyethylene in controlled-stress uniaxial extensional flow. *Journal of Rheology*, 55(5):925–937, 2011.

[19] A. Y Malkin, A Arinstein, and V. G Kulichikhin. Polymer extension flows and instabilities. *Progress in Polymer Science*, 39(5):959–978, 2014.

[20] Y Wang, P Boukany, S.-Q Wang, and X Wang. Elastic breakup in uniaxial extension of entangled polymer melts. *Physical Review Letters*, 99(December):1–4, 2007.

[21] V. C Barroso and J. M Maia. Time dependent effects on the rupture of molten linear polymers in extension. *Journal of Non-Newtonian Fluid Mechanics*, 126(2-3):93–103, mar 2005.

[22] V. C Barroso, R. J Andrade, and J. M Maia. An experimental study on the criteria for failure of polymer melts in uniaxial extension: The test case of a polyisobutylene

melt in different deformation regimes. *Journal of Rheology*, 54(3):605–618, 2010.

[23] Y Wang and S.-Q Wang. From elastic deformation to terminal flow of a monodisperse entangled melt in uniaxial extension. *Journal of Rheology*, 52(2008):1275–1290, 2008.

[24] Y Wang and S.-Q Wang. Rupture in rapid uniaxial extension of linear entangled melts. *Rheologica Acta*, 49: 1179–1185, 2010.

[25] Y Wang and S.-Q Wang. Salient features in uniaxial extension of polymer melts and solutions: Progressive loss of entanglements, yielding, non-Gaussian stretching, and rupture. *Macromolecules*, 44:5427–5435, 2011.

[26] G Liu, H Sun, S Rangou, K Ntetsikas, A Avgeropoulos, and S.-Q Wang. Studying the origin of strain hardening: Basic difference between extension and shear. *Journal of Rheology*, 57(1):89, 2013.

[27] A Bach, H. K Rasmussen, and O Hassager. Extensional viscosity for polymer melts measured in the filament stretching rheometer. *Journal of Rheology*, 47(2): 429, 2003.

[28] H. K Rasmussen, J. K Nielsen, A Bach, and O Hassager. Viscosity overshoot in the start-up of uniaxial elongation of low density polyethylene melts. *Journal of Rheology*, 49(2):369, 2005.

[29] D. M Hoyle and S. M Fielding. Criteria for extensional necking instability in complex fluids and soft solids. Part II: imposed stress and force protocols. *Journal of Rheology*, 60:XXX–XXX, 2016

[30] S. M Fielding, P Sollich, and M. E Cates. Ageing and Rheology in Soft Materials. *Journal of Rheology*, 323 (2000):54, 1999.

[31] P Sollich, F Lequeux, P Hébraud, and M. E Cates. Rheology of Soft Glassy Materials. *Physical Review Letters*, 78(10):2020–2023, mar 1997.

[32] M. E Cates and P Sollich. Tensorial constitutive models for disordered foams, dense emulsions, and other soft nonergodic materials. *Journal of Rheology*, 48(1):193, 2004.

[33] C. J. S Petrie. Considère reconsidered: Necking of polymeric liquids. *Chemical Engineering Science*, 64(22): 4693–4700, nov 2009.

[34] M Considère. Memoire sur l'emploi du fer et de l'acier dans les constructions. *Ann. Ponts Chaussees*, 9:574, 1885.

[35] O Hassager, M. I Kolte, and M Renardy. Failure and nonfailure of fluid filaments in extension. *Journal of Non-Newtonian Fluid Mechanics*, 76(1-3):137–151, apr 1998.

[36] G. H McKinley and O Hassager. The Considere Condition and Rapid Stretching of Linear and Branched Polymer Melts. *Journal of Rheology*, 43(5):1195–1212, 1999.

[37] J Hutchinson and K Neale. Influence of strain-rate sensitivity on necking under uniaxial tension, 1977.

[38] Y Ide and J. L White. Investigation of failure during elongational flow of polymer melts. *Journal of Non-Newtonian Fluid Mechanics*, 2:281–298, 1977.

[39] D. O Olagunju. A 1-D theory for extensional deformation of a viscoelastic filament under exponential stretching. *Journal of Non-Newtonian Fluid Mechanics*, 87:27–46, 1999.

[40] D. O Olagunju. Extensional flow of a viscoelastic filament governed by the FENE-CR model. *International Journal of Non-Linear Mechanics*, 46(1):73–78, 2011.

[41] Y. M Joshi and M. M Denn. Rupture of entangled polymeric liquids in elongational flow. *Journal of Rheology*, 47(1):291–298, 2003.

[42] Y. M Joshi and M. M Denn. Rupture of entangled polymeric liquids in elongational flow with dissipation. *Journal of Rheology*, 48(3):591–598, 2004.

[43] A. Y Malkin and C. J. S Petrie. Some conditions for rupture of polymer liquids in extension. *Journal of Rheology*, 41(1):1–25, jan 1997.

[44] H. K Rasmussen. Catastrophic failure of polymer melts during extension. *Journal of Non-Newtonian Fluid Mechanics*, 198:136–140, 2013.

[45] P. P Bhat, S Appathurai, M. T Harris, M Pasquali, G. H McKinley, and O. a Basaran. Formation of beads-on-a-string structures during break-up of viscoelastic filaments. *Nature Physics*, 6(8):625–631, jun 2010.

[46] M Cromer, L. P Cook, and G. H McKinley. Extensional flow of wormlike micellar solutions. *Chemical Engineering Science*, 64(22):4588–4596, 2009.

[47] L Eastgate, J. S Langer, and L Pechenik. Dynamics of Large-Scale Plastic Deformation and the Necking Instability in Amorphous Solids. *Physical Review Letters*, 90 (4):045506, jan 2003.

[48] S. M Fielding. Criterion for Extensional Necking Instability in Polymeric Fluids. *Physical Review Letters*, 107 (25):258301, dec 2011.

[49] D. M Hoyle and S. M Fielding. Age-Dependent Modes of Extensional Necking Instability in Soft Glassy Materials. *Physical Review Letters*, 114(15):158301, 2015.

[50] C Clasen, J Eggers, M. a Fontelos, J Li, and G. H McKinley. The beads-on-string structure of viscoelastic threads. *Journal of Fluid Mechanics*, 556:283, may 2006.

[51] M Tembely, D. C Vadillo, M. R Mackley, and A Soucemarianadin. The matching of a one-dimensional numerical simulation and experiment results for low viscosity Newtonian and non-Newtonian fluids during fast filament stretching and subsequent break-up. *Journal of Rheology*, 56(1):159–183, 2012.

[52] D. C Vadillo, M Tembely, N. F Morrison, O. G Harlen, M. R Mackley, and A Soucemarianadin. The matching of polymer solution fast filament stretching, relaxation, and break up experimental results with 1D and 2D numerical viscoelastic simulation. *Journal of Rheology*, 56(6):1491–1516, 2012.

[53] M. F Webster, H Matallah, K Sujatha, and M. J Banaai. Numerical modelling of step-strain for stretched filaments. *Journal of Non-Newtonian Fluid Mechanics*, 151:38–58, 2008.

[54] C McIlroy and O. G Harlen. Modelling capillary breakup of particulate suspensions. *Physics of Fluids*, 26(3): 033101, mar 2014.

[55] P. P Bhat, O. a Basaran, and M Pasquali. Dynamics of viscoelastic liquid filaments: Low capillary number flows. *Journal of Non-Newtonian Fluid Mechanics*, 150: 211–225, 2008.

[56] M Renardy. Similarity solutions for jet breakup for various models of viscoelastic fluids. *Journal of Non-Newtonian Fluid Mechanics*, 104(1):65–74, apr 2002.

[57] J Eggers and E Villermaux. Physics of liquid jets. *Reports on Progress in Physics*, 71(3):036601, mar 2008.

[58] C Ligoure and S Mora. Fractures in complex fluids: the case of transient networks. *Rheologica Acta*, 52(2):91–114, jan 2013.

[59] C. H Rycroft and F Gibou. Simulations of a stretching bar using a plasticity model from the shear transforma-

tion zone theory. *Journal of Computational Physics*, 231 (5):2155–2179, mar 2012.

[60] H. K Rasmussen and A Bach. On the bursting of linear polymer melts in inflation processes. *Rheologica Acta*, 44 (5):435–445, apr 2005.

[61] R. G Larson. *Constitutive equations for polymer melts and solutions*. Butterworth Publishers, Stoneham, 1988.

[62] M Chilcott and J Rallison. Creeping flow of dilute polymer solutions past cylinders and spheres. *Journal of Non-Newtonian Fluid Mechanics*, 29:381–432, 1988.

[63] A. E Likhtman and R. S Graham. Simple constitutive equation for linear polymer melts derived from molecular theory: RoliePoly equation. *Journal of Non-Newtonian Fluid Mechanics*, 114(1):1–12, sep 2003.

[64] M. E Cates. Nonlinear viscoelasticity of wormlike micelles (and other reversibly breakable polymers). *The Journal of Physical Chemistry*, 94(1):371–375, jan 1990.

[65] M Doi and S Edwards. *The Theory of Polymer Dynamics*. Oxford University Press, Oxford, 1986.

[66] G Marrucci. Dynamics of entanglements: A nonlinear model consistent with the Cox-Merz rule. *Journal of Non-Newtonian Fluid Mechanics*, 62(2-3):279–289, 1996.

[67] G Ianniruberto and G Marrucci. Convective constraint release (CCR) revisited. *Journal of Rheology*, 58(1):89, 2014.

[68] G Ianniruberto and G Marrucci. Do Repeated Shear Startup Runs of Polymeric Liquids Reveal Structural Changes? *ACS Macro Letters*, 3(6):552–555, jun 2014.

[69] T. C. B McLeish and R. G Larson. Molecular constitutive equations for a class of branched polymers: The pom-pom polymer. *Journal of Rheology*, 42(February): 81, 1998.

[70] R. J Blackwell, T. C. B McLeish, and O. G Harlen. Molecular dragstrain coupling in branched polymer melts. *Journal of Rheology*, 44(1):121, 2000.

[71] M. G Forest and Q Wang. Change-of-type behavior in viscoelastic slender jet models. *Theoretical and Computational Fluid Dynamics*, 2(1):1–25, 1990.

[72] M. M Denn, C. J. S Petrie, and P Avenas. Mechanics of steady spinning of a viscoelastic liquid. *AIChE Journal*, 21(4):791–799, 1975.

[73] Note1. This arises because GW_{zz} and σ_{E} do not coincide in this regime: instead W_{xx} and W_{zz} are of comparable size and both contribute to σ_{E}. Recall that our derivation of the criterion above assumed $W_{zz} \equiv Z$ to be large compared to all other components of $\boldsymbol{W}$.

[74] Note2. This quantitative discrepancy arises because in the Pom-pom model the viscoelastic tensile stress depends not only on $\boldsymbol{W}$ but also on the auxiliary variable λ. Our derivation of onset criterion assumed the viscoelastic stress to be given simply by GW_{zz}.

[75] W. M. H Verbeeten, G. W. M Peters, and F. P. T Baaijens. Numerical simulations of the planar contraction flow for a polyethylene melt using the XPP model. *Journal of Non-Newtonian Fluid Mechanics*, 117(2-3):73–84, feb 2004.

[76] V Entov and E Hinch. Effect of a spectrum of relaxation times on the capillary thinning of a filament of elastic liquid. *Journal of Non-Newtonian Fluid Mechanics*, 72 (1):31–53, sep 1997.

[77] Y. M Stokes, E. O Tuck, and L. W Schwartz. Extensional fall of a very viscous fluid drop. *Quarterly Journal of Mechanics and Applied Mathematics*, 53:565–582, 2000.

[78] W. H Press, S. A Teukolsky, W. T Vetterling, and B. P Flannery. *Numerical Recipes 3rd Edition: The art of Scientific Computing*. Cambridge University Press, New York, 2007.

[79] X Zhu and S.-Q Wang. Mechanisms for different failure modes in startup uniaxial extension: Tensile (rupture-like) failure and necking. *Journal of Rheology*, 57(1):223, 2013.

[80] C Luap, C Müller, T Schweizer, and D. C Venerus. Simultaneous stress and birefringence measurements during uniaxial elongation of polystyrene melts with narrow molecular weight distribution. *Rheologica Acta*, 45(1): 83–91, sep 2005.

[81] H. K Rasmussen and O Hassager. The role of surface tension on the elastic decohesion of polymeric filaments. *Journal of Rheology*, 45(2):527, 2001.

[82] A Bonito, M Picasso, and M Laso. Numerical simulation of 3D viscoelastic flows with free surfaces. *Journal of Computational Physics*, 215(2):691–716, jul 2006.

[83] D. W Auhl, J Ramirez, A. E Likhtman, P Chambon, and C Fernyhough. Linear and nonlinear shear flow behavior of monodisperse polyisoprene melts with a large range of molecular weights. *Journal of Rheology*, 52(3):801, 2008.

[84] M Doi and T Ohta. Dynamics and rheology of complex interfaces. I. *The Journal of Chemical Physics*, 95(2): 1242, 1991.

Appendix A: Constitutive models

We now detail the constitutive models used in our numerical calculations. As discussed in Sec. III B of the main text, in each case the viscoelastic stress $\boldsymbol{\Sigma}$ can be written as the product of a constant modulus G and a tensorial function $\boldsymbol{S}$ of a dimensionless microstructural conformation tensor $\boldsymbol{W}$, together with any other microscopic variables $\lambda, Q, \cdots$ relevant to the fluid under consideration:

$$\boldsymbol{\Sigma} = G\boldsymbol{S}(\boldsymbol{W}, \lambda, Q, \cdots). \tag{A.1}$$

The dynamics of the conformation tensor is then specified by a differential equation of the general form

$$\frac{D\boldsymbol{W}}{Dt} = \boldsymbol{f}(\nabla \boldsymbol{v}, \boldsymbol{W}, \lambda, Q \cdots), \tag{A.2}$$

with counterpart scalar equations for the dynamics of $\lambda, Q, \cdots$, of the same differential form.

For notational convenience we define the Lagrangian derivative

$$\frac{D\boldsymbol{W}}{Dt} = \frac{\partial \boldsymbol{W}}{\partial t} + \mathbf{v} \cdot \nabla \boldsymbol{W}, \tag{A.3}$$

and the upper convected derivative

$$\overset{\nabla}{\mathbf{W}} = \frac{D\boldsymbol{W}}{Dt} - \boldsymbol{W} \cdot \mathbf{K} - \mathbf{K}^T \cdot \boldsymbol{W}, \tag{A.4}$$

with velocity gradient tensor $\mathbf{K}_{\alpha\beta} = \partial_\alpha v_\beta$.

1. Oldroyd B model

The phenomenological Oldroyd B model represents each polymer chain in a dilute polymer solution as a simplified dumbbell comprising two beads connected by a Hookean spring. The relevant conformation tensor $\boldsymbol{W} = \langle \boldsymbol{RR} \rangle$ is then the ensemble average $\langle\rangle$ of the outer dyad of the dumbbell end-to-end vector $\boldsymbol{R}$, which is taken to have unit length in the absence of flow.

The viscoelastic stress

$$\boldsymbol{\Sigma} = G\left(\boldsymbol{W} - \mathbf{I}\right), \tag{A.5}$$

with a constant modulus G (set by the thermal energy $k_{\mathrm{B}}T$, and the volume density of dumbbells.) In addition to the Hookean spring force, each bead also experiences viscous drag against the solvent [61], and stochastic thermal fluctuations. With these dynamics, the conformation tensor obeys

$$\overset{\nabla}{\mathbf{W}} = -\frac{1}{\tau}\left(\mathbf{W} - \mathbf{I}\right), \tag{A.6}$$

with a characteristic relaxation time τ (set by the thermal energy, the bead radius, and the solvent viscosity).

As discussed in the main text, for a sustained imposed extensional strain rate $\dot{\epsilon} > 1/2\tau$ the Oldroyd B model displays an extensional catastrophe in which the dumbbells stretch out indefinitely and the extensional stress grows indefinitely. The constitutive curve is accordingly undefined for $\dot{\epsilon} > 1/2\tau$.

2. FENE-CR model

The phenomenological FENE-CR model regularises the extensional catastrophe of the Oldroyd B model by insisting that the extension of the polymer chains (dumbbells) must remain finite in practice at all deformation rates. It does so by replacing the Hookean spring law with a non-linear spring law [62], in which the extensional stress

$$\boldsymbol{\Sigma} = Gf(\boldsymbol{W})\left(\boldsymbol{W} - \mathbf{I}\right), \tag{A.7}$$

and the conformation tensor obeys

$$\overset{\nabla}{\boldsymbol{W}} = -\frac{1}{\tau}f(\boldsymbol{W})\left(\boldsymbol{W} - \mathbf{I}\right). \tag{A.8}$$

Here

$$f\left(\boldsymbol{W}\right) = \frac{L^2}{L^2 - R^2} = \frac{1}{1 - \delta T/3}, \tag{A.9}$$

in which $3R^2 = T = tr(\boldsymbol{W})$ and L is a parameter that sets the maximum length of the polymer chains. We write $L = \delta^{-1/2}$ and work instead with the parameter δ. (The limit $\delta \to 0$ corresponds to Oldroyd B dynamics with infinite extensibility.) The FENE-CR model has a well defined extensional constitutive curve at all strain rates $\dot{\epsilon}$, with a finite limiting extensional viscosity $G\tau/\delta$ as $\dot{\epsilon} \to \infty$

3. Giesekus model

The phenomenological Giesekus model was developed in an attempt to model more concentrated polymers solutions and melts, starting from the simple dumbbell model for dilute solutions. It invokes an anisotropic drag such that the relaxation time of a molecule (dumbbell) is altered when the surrounding molecules (dumbbells) are oriented [61]. The viscoelastic stress

$$\boldsymbol{\Sigma} = G(\boldsymbol{W} - \mathbf{I}), \tag{A.10}$$

with the conformation tensor obeying the dynamics

$$\overset{\nabla}{\boldsymbol{W}} = -\frac{1}{\tau}\left(\boldsymbol{W} - \mathbf{I}\right) - \frac{\alpha}{\tau}\left(\boldsymbol{W} - \mathbf{I}\right)^2. \tag{A.11}$$

The parameter α controls the degree of drag anisotropy, and must lie in the range $0 \leq \alpha \leq 1$. The limit $\alpha \to 0$ recovers Oldroyd B dynamics. For $\alpha > 0$ the Giesekus model regularises the extensional catastrophe of the Oldroyd B model and has a well defined constitutive curve at all extension rates, with a finite limiting extensional viscosity $G\tau/\alpha$ in the limit $\dot{\epsilon} \to \infty$. For matched (small) values of α and δ the steady state extensional constitutive curves of the Giesekus and FENE-CR models coincide. As shown in the main text, their extensional *dynamics* also closely correspond, though with some quantitative differences.

Model	Non-linear parameters
Oldroyd-B	-
Giesekus	$\alpha = 0.001$
FENE-CR	$\delta = 0.001$
non-stretch Rolie-Poly	$\beta = 0.0$
stretch Rolie-Poly	$\beta = 0.0$, $\delta = -0.5$, $\tau_R = 0.00833$ $(Z = 40)$
finite-stretch Rolie-Poly	$\beta = 0.0$, $\delta = -0.5$, $\tau_R = 0.00833$ and $f = 0.000625$ $(Z = 40)$
Pom-pom (PP1)	$\tau_s = 0.1$ and $q = 40$
Pom-pom (PP2)	$\tau_s = 0.1$ and $q = 5$
Doi-Ohta fluidity	$\tau_w = 1000$ and $\mu = 0.1$

TABLE I. Parameter values used in our numerical studies of the constitutive models. The solvent viscosity is taken as $\eta = 0.001$ in all cases.

4. Rolie-Poly model of linear polymers

The three models presented so far are phenomenological in nature, based on simple dumbbell descriptions. The Rolie-Poly model [63] provides a more microscopically motivated description of concentrated solutions and melts of linear polymers. As discussed in the main text, it is based on the tube theory of Doi and Edwards [65] in which any given polymer chain is dynamically restricted by a confining tube of topological entanglements with the surrounding chains, and is assumed to refresh its configuration by the basic dynamical process of reptation, chain stretch relaxation and convective constraint release [66–68] (CCR). Incorporating these process into a differential constitutive equation for the dynamics of $\boldsymbol{W} = \langle \boldsymbol{RR} \rangle$, with $\boldsymbol{R}$ the end-to-end vector of a polymer chain, gives

$$\overset{\nabla}{\boldsymbol{W}} = -\frac{1}{\tau_d}(\boldsymbol{W} - \mathbf{I}) - \frac{2}{\tau_s(1 - fT/3)}\left(1 - \sqrt{\frac{3}{T}}\right)\left[\boldsymbol{W} + \beta\left(\frac{T}{3}\right)^{\delta}(\boldsymbol{W} - \mathbf{I})\right]. \tag{A.12}$$

Here τ_d and τ_s are respectively the characteristic timescales of reptation and of chain-stretch relaxation. These are assumed to have the ratio

$$\frac{\tau_d}{\tau_s} = 3Z, \tag{A.13}$$

where Z is the number of entanglements per chain.

In our numerics we take $Z = 40$, corresponding to a well entangled system as used for example in Ref. [83]. The parameter β sets the degree of CCR. (Note that the β used here is distinct from the one used in the definition of the toy model in the main text, which is also repeated in Eqn. A.28 below.) Following [63] we take $\beta = 0.0$ and $\delta = -1/2$. The factor $(1 - fT/3)$ accounts for finite chain extensibility, as in Eqn. A.7 for the FENE-CR model. This gives a bounded tensile polymer stress of $3G/f$ in the limit $\dot{\epsilon} \to \infty$.

For highly entangled chains (large Z) the chain-stretch relaxes quickly quickly on the timescale of reptation, $\tau_s \ll \tau_d$. For imposed flow rates $\dot{\epsilon} \ll 1/\tau_s$ it is then convenient to take the limit $\tau_s \to 0$ upfront and work with the non-stretching form of the Rolie-Poly, in which the conformation dynamics obey

$$\overset{\nabla}{\boldsymbol{W}} = -\frac{1}{\tau_d}(\boldsymbol{W} - \mathbf{I}) - \frac{2}{3}\mathbf{K} : \boldsymbol{W}\left(\boldsymbol{W} + \beta(\boldsymbol{W} - \mathbf{I})\right). \tag{A.14}$$

This also recovers the reptation-reaction model of wormlike micelles [64] for $\beta = 0$.

In this non-stretching limit and for $\beta = 0.0$ (as used in our numerics) the quantity $\sigma = W_{zz} - W_{xx}$, which determines the tensile stress as $G\sigma$, evolves according to

$$\frac{D\sigma}{Dt} = \dot{\varepsilon}\left(3 + \sigma - \frac{2}{3}\sigma^2\right) - \frac{1}{\tau}\sigma, \tag{A.15}$$

This has the basic form proposed for the simplified toy version of the Rolie-Poly model at the end of Sec. V with β in that toy model set equal to 1 here. (Note that β in the toy model written in the main text is different from the β used in this appendix for the tensorial Rolie-Poly model. Note also that the prefactor to the linear loading term in Eqn A.15 is half that in the toy model in the main text. This however has no effect on the qualitative behaviour.)

5. Pom-pom model of branched polymers

The models discussed so far pertain to polymeric fluids with molecules of linear topology. We now turn to entangled branched polymers in which each molecule is assumed to comprise a linear backbone with an equal

number of arms q attached to each end, as modelled by the Pom-pom model [69, 70]. The relaxation of the arms is considered fast compared to that of the backbone, and so is not ascribed its own dynamics but acts as an additional drag, which slows the relaxation of the backbone. The two dominant relaxation processes in the Pom-pom model are therefore taken to be backbone reorientation, with a characteristic timescale τ_b; and backbone stretch relaxation, with timescale τ_s. These two timescales are assumed to be in the ratio

$$\frac{\tau_b}{\tau_s} = Z_b \phi_b, \tag{A.16}$$

where Z_b is the number of entanglements along the backbone and

$$\phi_b = \frac{Z_b}{Z_b + 2qZ_a}, \tag{A.17}$$

with Z_a the number of entanglements along each arm such that ϕ_b is the fraction of material in the backbone compared that in the molecule as a whole.

The viscoelastic stress

$$\mathbf{\Sigma} = 3G\lambda^2 \left(\mathbf{W} - \frac{1}{3}\mathbf{I} \right), \tag{A.18}$$

in which $\boldsymbol{W}$ is a conformation tensor characterising the backbone orientation and λ encodes the backbone stretch. McLeish and Larson [69] modelled the backbone orientation both using the full Doi-Edwards tensor, and also in a simpler a differential approximation, which we adopt here, taking:

$$\mathbf{W} = \frac{\mathbf{A}}{\mathrm{tr}(\mathbf{A})}, \tag{A.19}$$

with the dynamics of $\mathbf{A}$ obeying the Maxwell model, Eqn. A.6, with relaxation time τ_b. The backbone stretch evolves according to

$$\frac{D\lambda}{Dt} = \lambda \mathbf{K} : \mathbf{W} - \frac{1}{\tau_s} (\lambda - 1) \, e^{\nu^* (\lambda - 1)} \quad \text{for} \quad \lambda \leq q, \tag{A.20}$$

where $\nu^* = 2/(q-1)$, subject to an initial condition $\lambda(0) = 1$. A hard cutoff is then imposed once $\lambda = q$, because the extent of backbone stretch is taken to be entropically bounded by the number of arms attached to each end of the backbone, placing an upper bound on the tensile stress of $3Gq^2$. As shown in the main text, the imposition of the hard cutoff leads to catastrophically fast necking via the elastic Considère mode in this original version of the Pom-pom model. We shall also consider a modified model [75] in which the hard cutoff is removed, such that λ obeys Eqn. A.20 for all values, and find much more gradual necking dynamics.

In the main text we present results for two different sets of model parameters. The first, which we call PP1, has a high number of arms, $q = 40$. We take $Z_b \phi_b = 10.0$, such that $\tau_s = \tau_d/10.0$, giving a less wide separation of the reorientation and stretch times for PP1 than in our studies of the Rolie-Poly model, consistent with the expectation that stretch arises more readily in branched polymers due to the drag of the side arms. The second set of model parameters, which we call PP2, assumes fewer arms, $q = 5$, but still with $\tau_s = \tau_d/10.0$.

6. Fluidity model of soft glassy materials

We adopt a simplified tensorial fluidity model [49, 84] of soft glassy materials [31, 32]. This considers a local density function $f(\mathbf{n})$ for the area (per unit volume) of droplet interfaces normal to $\mathbf{n}$, with a normalisation

$$Q = \int d\mathbf{n} f(\mathbf{n}). \tag{A.21}$$

The viscoelastic stress

$$\Sigma = G\boldsymbol{W} \tag{A.22}$$

with a conformation variable

$$\boldsymbol{W} = \int d\mathbf{n} (\mathbf{nn} - \tfrac{1}{3}\mathbf{I}). \tag{A.23}$$

The conformation variable has the dynamics

$$\overset{\nabla}{\boldsymbol{W}} = \frac{2}{3} Q \mathbf{D} - \boldsymbol{W} : \mathbf{K} \left(\frac{2}{3}\mathbf{I} + \frac{\boldsymbol{W}}{Q} \right) - \frac{1}{\tau} Q \boldsymbol{W}, \tag{A.24}$$

while Q obeys

$$\frac{DQ}{Dt} = \mathbf{K} : \boldsymbol{W} - \frac{1}{\tau} \mu Q^2. \tag{A.25}$$

Here μ is a phenomenological parameter, which lies in the range $0 \leq \mu \leq 1$ [84].

The relaxation timescale τ is assigned its own dynamics according to

$$\frac{D\tau}{Dt} = 1 - \sqrt{2\mathbf{D} : \mathbf{D}} \, (\tau - \tau_0), \tag{A.26}$$

where $\mathbf{D}$ is the symmetric part of the velocity gradient tensor $\mathbf{K}$ and τ_0 is a microscopic time, set to unity in our units. The first term on the right hand side captures ageing in the absence of flow, giving a relaxation timescale $\tau \sim t_\mathrm{w}$ that increases as a function of the sample age, *i.e.*, the time since sample preparation (assuming $\tau = \tau_0$ for a freshly prepared sample). An applied flow (second term) can then arrest ageing and restore a steady state relaxation timescale set by the inverse flow rate.

We solve the above equations assuming an initial undeformed sample of age t_w (such that the initial age $\tau(t=0) = t_\mathrm{w}$). The initial conditions for Q is a function of μ [49].

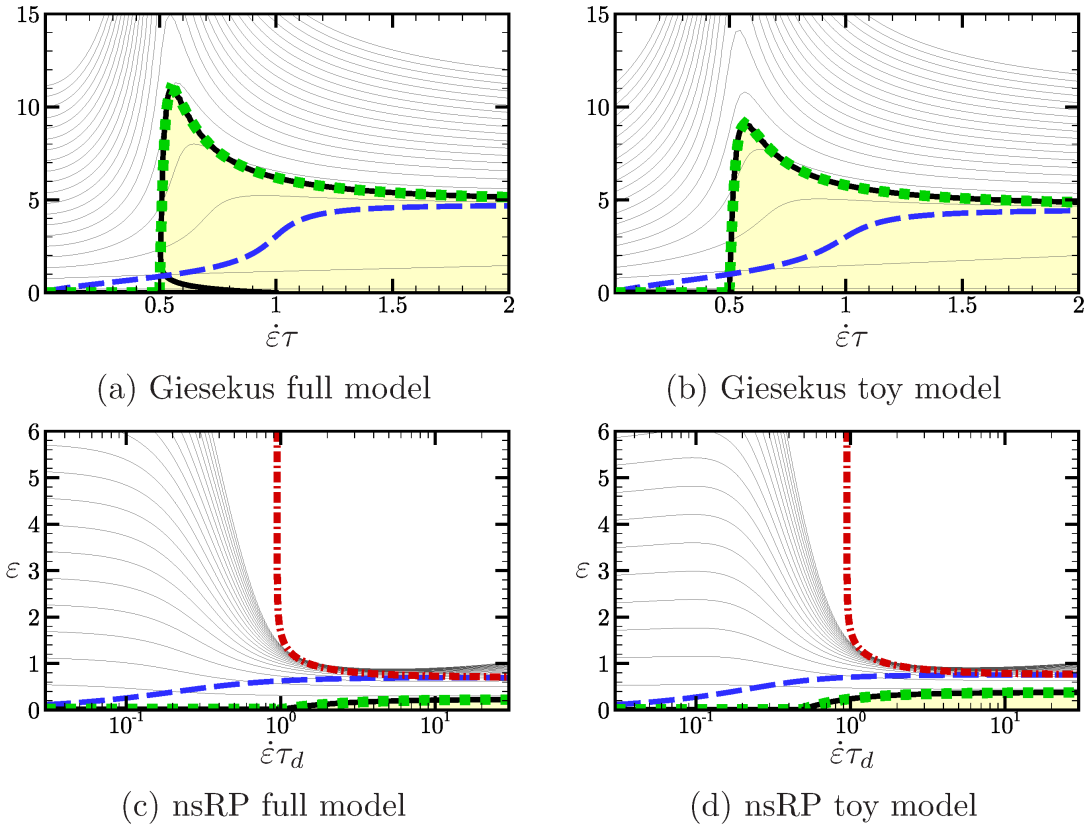

FIG. 11. Giesekus (top) and non-stretch Rolie-Poly (bottom) full (left) and toy(right) model comparisons. For both full and toy Giesekus we use $\alpha = 0.001$. For the non-stretch Rolie-Poly model this is equivalent to taking $\beta = 2/3$ in the toy model.

7. Toy scalar constitutive models

At the end of Sec. V we introduced a simplified, generalised, scalarised toy constitutive model that considers only the tensile component of the viscoelastic stress $\Sigma = GZ$ with dynamics

$$\partial_t Z + \boldsymbol{v}.\nabla Z = \dot{\epsilon} f(Z) - \frac{1}{\tau} g(Z), \tag{A.27}$$

in which

$$f(Z) = 3 + 2Z - \beta Z^2, \tag{A.28}$$

and

$$g(Z) = Z + \alpha Z^2. \tag{A.29}$$

It was in this model that we analytically derived our criteria for the onset of necking. We also noted in the main text that this toy model is capable of giving an excellent approximation to the extensional necking dynamics of the full tensorial Oldroyd B model ($\alpha = \beta = 0$); the Giesekus model ($\alpha \neq 0, \beta = 0$); and the Rolie-Poly model without chain stretch ($\alpha = 0, \beta \neq 0$). This is confirmed in Fig. 11, which shows the counterpart of the results of the full constitutive models of Fig. 3, comparing the full tensorial Giesekus model with its toy scalar counterpart, and likewise the Rolie-Poly model without chain stretch with its toy counterpart. This excellent comparison between the scalar toy models and their full tensorial counterparts lends additional confidence to our having derived our analytical criteria for necking within the scalar toy model.

To justify our focusing on just one component of the conformation tensor in this toy model, we have checked that in the Giesekus model (and finite-stretch Rolie-Poly model) in the vicinity of the pronounced nose-shaped curve denoting the onset of instability we have $W_{zz} \gg W_{xx}$, justifying our use of just one component $Z = W_{zz} - W_{xx} \approx W_{zz}$ in that case. In the non-stretch Rolie-Poly model the dynamics can exactly be written in terms of just one component, $Z = W_{zz} - W_{xx}$, which separately justifies our use of just one component in the toy version of that model. These facts are consistent with the excellent agreement between our numerical results obtained between the full models and their toy counterparts in Fig. 11.